Alveolar epithelium propagates mechanical signals that control multi-cellular homeostasis in the lung

Chen Shen[1,2], Michael P. Morley[1,2,3], Sarah E. Schaefer[1,2], Gan Zhao[1,2], Joseph D. Planer[1,2], Ullas V. Chembazhi[1,2], Dakota L. Jones[1,2], Mijeong Kim[1,2], Yun Ying[1,2], Su Zhou[1,2], Shanru Li[1,2], Hannah Hallquist[1,2], Ana Lange[1,2], Maria C. Basil[1,2,3], Edward E. Morrisey[1,2,3,4,*]

[1]Department of Medicine, Perelman School of Medicine, University of Pennsylvania, Philadelphia, PA, USA.

[2]Penn-CHOP Lung Biology Institute, Perelman School of Medicine, University of Pennsylvania, Philadelphia, PA, USA.

[3]Penn Cardiovascular Institute, University of Pennsylvania, Philadelphia, PA, USA.

[4]Department of Cell and Developmental Biology, Perelman School of Medicine, University of Pennsylvania, Philadelphia, PA, USA.

***Corresponding author:**

Edward E. Morrisey
Department of Medicine
University of Pennsylvania
Smilow Translational Research Center, Room 11-124
3400 Civic Center Blvd
Philadelphia, PA 19104-5129
Email: emorrise@pennmedicine.upenn.edu

Abstract

Respiratory motion imposes a constant mechanical strain that has important but poorly defined impact on tissue niches in the lung. We developed a reversible bronchial ligation model to induce and reverse unilateral blockade of lung mechanical motion *in vivo* and show that this leads to transcriptomic changes in multiple cell lineages that are not normalized upon reinitiation of respiratory motion. Perturbation of mechanosignaling specifically in alveolar epithelial type I (AT1) cells alters the transcriptomic state and fate of their niche neighbors, demonstrating that AT1 cells act as a node that propagates a mechanical cascade throughout the lung alveolus. Mechanically perturbed AT1 cells induce a distinct capillary endothelial cell state that persists after reactivation of respiratory motion, which is mediated by an integrin/TGF-β network within the alveolus that is vulnerable to pharmacological intervention. Importantly, AT1 mechanosignaling and intercellular communication are altered in chronic human lung diseases, highlighting the critical role of an AT1-driven mechanosensing network in lung disease biology. Thus, mechanosensing cells propagate biophysical signals that regulate tissue function and program tissue responses in disease.

Introduction

Pulmonary gas exchange occurs within the alveoli, the elastic air sacs in the distal lung. During respiration, the alveoli are subjected to a constant, cyclical mechanical strain, which facilitates gas diffusion across a tight interface formed by the alveolar epithelium and the endothelium of the adjacent capillary plexus, with a fused basement membrane in between these two cells[1,2]. In lung diseases, this mechanical load is often disrupted, represented by damaged alveolar tissue architecture and compliance[3]. Despite the importance of pulmonary mechanical homeostasis, how these forces regulate cell behavior and fate within the gas exchange interface and the impact this has on tissue structure and function is poorly understood.

Recent studies have shown that mechanical forces are essential for maintaining alveolar epithelial cell fate and function[4-7]. Alveolar type II (AT2) epithelial progenitors require proper mechanical forces to differentiate into alveolar type I (AT1) cells, which facilitate alveolar gas exchange with the capillary endothelium[4-7]. AT1 cells exhibit high mechanosignaling activity and depend on mechanotransduction to maintain their identity, with loss-of-function mechanosignaling leading to their reprogramming into AT2 cells[4,8]. We have previously demonstrated that AT1 cells are responsive to respiration-mediated mechanical forces *in vivo* by surgical blockade of lung motion[4]. Perturbed respiratory motion caused AT1 cells to reprogram into AT2 cells, mimicking the

phenotype observed upon attenuation of mechanotransduction in AT1 cells through loss of Hippo signaling and actin dynamics[4,8]. However, in all of these models, loss of mechanical signaling was permanent, which did not allow for the characterization of the impact that reinitiation of this signaling process would have on cell fate and tissue dynamics.

Here, we developed a reversible bronchial ligation model to induce temporary unilateral blockade of lung motion in mice, followed by restoration of respiratory movements, and used this model to characterize both transient and persistent alterations in cell fate and behavior induced by respiration-mediated mechanical forces. This model has allowed us to generate a tissue-wide mechanotransduction map in the lung at single-cell resolution. Analyses of our single-cell RNA sequencing (scRNAseq) dataset demonstrate that temporary respiratory blockade can lead to persistent cell transcriptomic alterations, which can occur through mechanisms beyond intrinsic mechanotransduction in cells. These analyses reveal that AT1 cells are a node for mechanotransduction in the lung alveolus that senses biophysical responses and propagates mechanical signals to other niche neighbors including AT2 epithelial, alveolar fibroblast, and CAP1 endothelial progenitors. Deregulation of mechanotransduction specifically in AT1 cells induces an irreversible, transcriptionally distinct CAP state via intercellular integrin/TGF-β signaling originated from AT1s. Human lung scRNAseq data indicate aberrant AT1 mechanosensing in chronic lung diseases, including opposing effects on chronic obstructive pulmonary disease (COPD) and idiopathic pulmonary fibrosis (IPF). Together, our findings demonstrate a pivotal role for an AT1 mechanosensing network that propagates a wave of signaling throughout the alveolus critical for maintaining tissue integrity and can be used to phenotype human lung diseases.

Results

Mechanical forces maintain multi-cellular homeostasis of the lung alveolus

To understand how cells in the lung respond to changes in mechanical forces, we developed a reversible bronchial ligation model to induce and reverse blockade in respiration-induced mechanical forces *in vivo* (**Fig. 1a**)[4]. In this model, the left main bronchus of mice is ligated by a micro-clip to temporarily restrain unilateral respiratory movements (Ligation, **Fig. 1a**), which can be later removed to restore respiratory motion (Reversed, **Fig. 1a**). Reversed lungs were found to be reinflated and their histological appearance by Hematoxylin and Eosin staining was relatively normal (**Extended Data Fig. 1a-b**). We performed sham, ligation, or reversed surgery in adult wildtype mice, isolated cells from the lungs and performed single-cell RNA sequencing (scRNA

seq) to determine transcriptomic changes in cells due to modulated mechanical forces (**Fig. 1b**). All expected cell types were successfully captured in the scRNAseq experiment and annotated (**Fig. 1c-f and Extended Data Fig. 1c**). We noticed altered transcriptome in various resident cell types within the alveolus in response to restrained respiration, especially in progenitor cells such as AT2 epithelial cells, CAP1 capillary endothelial cells and alveolar fibroblasts (**Fig. 1c-f**). Of note, not all transcriptomic changes in these cell types were fully normalized after restored respiratory motion. This suggests that disrupted mechanical forces can induce irreversible transcriptomic changes in the lung even after normalization of respiration, with a potential impact on progenitor cell function.

The facultative progenitor AT2 cells self-renew and differentiate into AT1 epithelial cells upon lung injury[9-13]. Prior studies have demonstrated that mechanical forces are critical for AT2-to-AT1 differentiation[4-7]. In addition, AT1 cells are sensitive to mechanical strain and can reprogram into AT2 cells in response to inhibited mechanical signaling[4,8]. Immunostaining of mouse lung tissues using antibodies against AT1- or AT2-specific marker showed that compared to the sham procedure, ligation induced a significant decrease in AT1 cell proportion, while AT2 cells showed an increased percentage (**Fig. 1g and Extended Data Fig. 2a**). This is similar to what we have previously shown and in line with AT1-to-AT2 reprogramming upon blocked mechanical forces. After the procedure is reversed, AT1 and AT2 cell percentages were normalized, likely through AT2-AT1 differentiation (**Fig. 1g**). Gene set enrichment analysis showed that Wnt and FGFR signaling that are essential for AT2 progenitor cell function were downregulated in AT2 cells in ligated mouse lungs but restored after reversal (**Extended Data Fig. 2b**)[12,14].

The lung capillary plexus and alveolar epithelium form a tight interface to facilitate efficient gas exchange[1,2]. Capillary endothelium (CAPs) is comprised of two distinct populations, CAP1 which are the proliferative progenitor subpopulation and CAP2 which exhibit a different phenotype consisting of increased expression of angiogenic genes[15,16]. The regeneration of CAPs has been shown to play a critical role in rebuilding lung tissue structure and function after acute injury and is driven largely by proliferation and differentiation of CAP1s[17-20]. To understand how progenitor CAPs respond to mechanical insults, we examined overall CAP proliferation by detecting cellular 5-ethynyl-2'-deoxyuridine (EdU) incorporation in mouse ligated lungs and those after reversed surgery (**Extended Data Fig. 3a-b**). We found that baseline EdU incorporation in CAPs was significantly reduced in the ligated mouse lungs (**Fig. 1h**). However, this was fully rescued when the ligation is reversed (**Fig. 1h**). Some CAP transcriptomic changes induced by ligation were

128 reversed by ligation removal, such as changes in TGF-β signaling (**Extended Data Fig. 3c**).
129 Together, these findings suggests that mechanical forces are essential for maintaining the multi-
130 cellular integrity and function of the lung alveolus (**Fig. 1i**).
131
132 **Cellular response to mechanical forces can be independent of intrinsic mechanosignaling**
133 One of the primary transducers of mechanical forces into cells is the Hippo pathway, which is
134 controlled by two essential transcription co-factors, Yes-associated protein (YAP) and
135 transcriptional coactivator with PDZ-binding motif (TAZ) (**Fig. 2a**)[21-23]. To evaluate the changes in
136 cellular mechanosignaling, a transcriptional score was generated for each cell type based on the
137 expression profile of 22 known YAP/TAZ target genes (mechanoscore) (**Fig. 2a**)[24]. In the
138 homeostatic lung, cells exhibit differential levels of mechanotransduction based on this score, with
139 AT1 cells and mesenchymal cells showing the highest mechanosignaling activity relative to other
140 cell types (mech-high cells, **Fig. 2b-d**). Using Euclidian distance analysis, we quantified
141 transcriptomic changes in lung cells after bronchial ligation and upon reversal, based on their
142 proximity to baseline gene expression profiles. Ligation-induced transcriptomic changes were
143 noted in various resident cell types within the alveoli, including AT1 cells and all mesenchymal
144 cells, consistent with their sensitivity to this perturbation (**Fig. 2e-f and Extended Data Fig. 4a-**
145 **b**)[4,25,26]. We noted that transcriptional alterations in mesenchyme cells persisted after reversed
146 surgery, whereas the AT1 cell transcriptome was largely normalized, suggesting AT1 cells are
147 highly adaptable to respiration-mediated mechanical forces (**Fig. 2e and Extended Data Fig.**
148 **4b**). Interestingly, some cells with low baseline mechanical activity (mech-low cells) also exhibited
149 an altered transcriptomic profile in response to perturbed mechanical forces, e.g. AT2 cells and
150 CAPs (**Fig. 2g-h and Extended Data Fig. 4a-b**). These changes were not distinct to
151 mechanotransduction, suggesting that biophysical forces can regulate gene expression and cell
152 state in these mech-low cells via mechanisms beyond classical mechanical signaling (**Fig. 2g-h**
153 **and Extended Data Fig. 4a-b**). Together, these studies reveal how biophysical forces are sensed
154 at both cell-intrinsic and -extrinsic levels to maintain tissue homeostasis in a mechanically loaded
155 organ such as the lung.
156
157 **AT1 cells are a node that propagates mechanical signaling cascades to neighboring cells**
158 **to control niche homeostasis**
159 Within the alveoli, the large squamous AT1 cells occupy over 90% of the surface area[1,2]. AT1 cells
160 are adjacent to many other cells in the alveolar niche, including AT2 cells and CAPs, which play
161 an essential role in lung structure and function and communicate with AT1 cells[1,2,27,28]. Loss of

162 mechanical signaling in AT1 cells, either by loss of the pivotal cytoskeleton assembly gene *Cdc42*
163 or through bronchial ligation, causes AT1 cells to reprogram into AT2 cells[4]. Therefore, we
164 genetically deleted *Cdc42* in AT1 cells (*Cdc42*$^{AT1\text{-}KO}$) to determine the impact from loss of
165 mechanosignaling in AT1 cells on their alveolar neighbor cells using scRNAseq (**Fig. 3a**). Whole
166 lung scRNAseq analysis revealed that loss of mechanotransduction in AT1 cells led to altered
167 transcriptome of specific neighboring cell types, including AT2 cells, CAP1s and alveolar
168 fibroblasts (**Fig. 3b-e and Extended Data Fig. 5a-b**), supporting the concept that AT1 cells are a
169 node of mechanotransduction in the lung.
170
171 To further understand the impact of AT1 mechanoresponses on adjacent CAPs, we subseted
172 CAPs from *Cdc42*$^{AT1\text{-}KO}$ scRNAseq data to analyze their transcriptomic profile at a higher
173 resolution (**Fig. 3b and f**). We identified a CAP state specific to *Cdc42*$^{AT1\text{-}KO}$ lungs (AT1-induced
174 CAP) that was characterized by enriched expression of a set of genes including *Ntrk2* and *Cd74*
175 (**Fig. 3f-g**). To validate the presence of these cells, we isolated cells from control or *Cdc42*$^{AT1\text{-}KO}$
176 mouse lungs and performed flow cytometry analyses using a Tropomyosin receptor kinase B
177 (TrkB) antibody to quantitate the percentage of *Ntrk2*$^{+}$ CAPs. We confirmed that loss of *Cdc42* in
178 AT1 cells led to the emergence of *Ntrk2*$^{+}$ CAPs in mouse lungs in a time-dependent manner (**Fig.
179 3h and Extended Data Fig. 6a**). In addition, tissue immunostaining using TrkB antibody validated
180 the presence of *Ntrk2*$^{+}$ AT1-induced CAPs in mouse ligated lungs (**Fig. 3i**). These results indicate
181 that AT1 cells can transmit their mechanosensitive responses to neighboring cells to mediate lung
182 tissue homeostasis (**Fig. 3j**).
183
184 **The AT1 mechanosensing-induced CAP state is permanent and functionally distinct**
185 Given the alteration in CAP gene expression upon loss of *Cdc42* in AT1 cells, we next asked
186 whether this also occurred upon blockade of respiratory motion. We reclustered the CAP
187 populations in the scRNAseq data from sham, ligated, or reversed mouse lungs to identify
188 alterations in cell states (**Fig. 1b-c and Fig. 4a**). CAP1 progenitors and the intermediate
189 CAP1_CAP2 cell state were significantly altered at the transcriptional level, losing their
190 homeostatic state upon respiratory blockade (**Fig. 4a-b**). Instead, we identified a distinct
191 population of CAPs that emerged in ligated mouse lungs and persisted after reversal (Ligation-
192 induced CAP), with enriched expression of a number of genes induced by inhibiting
193 mechanotransduction in AT1 cells, e.g. *Ntrk2* (**Fig. 4a-c, Extended Data Fig. 7a-b**). Moreover,
194 we found that there was a strong correlation between the transcriptome of Ligation-induced CAPs
195 and AT1-induced CAPs, suggesting that they represent similar cell states (**Fig. 4d**). We hereafter

196 termed these *Ntrk2*$^{+}$ CAPs as mechanically induced CAPs (miCAPs). The existence of miCAPs
197 was further validated in ligated and reversed mouse lungs by flow cytometry and tissue
198 immunostaining using TrkB antibody (**Fig. 4e-f**). Despite the persistence of miCAP state in the
199 reversed lung, we noted that these cells exhibited enhanced proliferation compared to TrkB^{-}
200 endothelial cells (ECs) during reversal of bronchial ligation (**Extended Data Fig. 3a and 8a-c**). To
201 determine the fate change of miCAPs in this process, we used *Ntrk2*$^{+}$ lineage tracing to track
202 miCAPs and noted that approximately 50% of the traced cells lost TrkB expression after
203 restoration of respiratory motion (**Fig. 4g and Extended Data Fig. 8d-i**). Interestingly, a similar
204 percentage of miCAPs were capable of differentiating into CAP2 cells upon ligation reversal (**Fig.
205 4h-i**). These results suggest that some miCAPs can differentiate into CAP2 cells during resolution
206 of lung motion blockade.
207
208 To investigate the cell of origin for the miCAPs, we utilized two previously validated lineage trace
209 mouse lines, *Kit*^{MerCreMer}*; R26R*^{tdTomato} and *Car4*^{CreERT2}*; R26R*^{tdTomato} to label CAP1s and CAP2s,
210 respectively, and track their cell state changes upon attenuated respiratory movements (**Fig. 4j**)[17].
211 CAP1- and CAP2-trace mice were given tamoxifen to initiate lineage tracing, followed by sham
212 or bronchial ligation surgery (**Fig. 4j**). Flow cytometry and IHC analyses indicated that both CAP1
213 and CAP2 lineage can give rise to miCAPs upon inhibition of respiratory motion (**Fig. 4k-l and
214 Extended Data Fig. 9a**).
215
216 To determine whether cell intrinsic mechanotransduction in CAP1 or CAP2 caused their state
217 switch to miCAPs, mouse lines were created to block intrinsic mechanotransduction in either
218 CAP1 or CAP2 by conditional knockout of *Cdc42* (*Cdc42*$^{CAP1\text{-}KO}$ or *Cdc42*$^{CAP2\text{-}KO}$, **Fig. 4m**). These
219 knockouts successfully attenuated mechanotransduction in CAPs, as indicated by decreased
220 expression of mechanosignaling target genes including *Ccn1*, *Ccn2* and *Ankrd1* (**Extended Data
221 Fig. 9b**)[24]. However, we did not observe the miCAP state arising from either CAP1 or CAP2
222 lineage upon cell intrinsic inhibition of mechanotransduction (**Fig. 4n and Extended Data. Fig.
223 9c**). Together, these findings indicate that this permanent miCAP state is functionally distinct and
224 its emergence is induced by defective mechanotransduction in neighboring AT1 cells.
225
226 **AT1-endothelial mechanotransduction requires integrin/TGF-β signaling**
227 To define the mechanisms by which AT1 cells sense and transmit mechanical signals to their
228 adjacent CAPs to induce the miCAP state, we analyzed the signaling pathways enriched in CAPs
229 from *Cdc42*$^{AT1\text{-}KO}$ mouse lungs using our scRNAseq data (**Fig. 3h and 5a**). The transforming

growth factor β (TGF-β) pathway was significantly upregulated in CAPs in response to *Cdc42*$^{AT1-KO}$ (**Fig. 5a**). Of note, TGF-β signaling was also enriched in CAPs from the ligated mouse lungs (**Extended Data Fig. 3c**). To validate altered TGF-β signaling in CAPs, we isolated CD31^{+} ECs from control or *Cdc42*$^{AT1-KO}$ mouse lungs by fluorescence-activated cell sorting (FACS) and examined phosphorylation of Suppressor of Mothers against Decapentaplegic (SMAD) proteins 2/3 (**Fig. 5b and Extended Data Fig. 10a**). Consistent with TGF-β signaling activation, phosphorylated SMAD2/3 in ECs from *Cdc42*$^{AT1-KO}$ mouse lungs was significantly increased relative to that from control (**Fig. 5b-c**)[29,30]. To assess the necessity of TGF-β signaling in the development of miCAP state, we genetically deleted the gene encoding TGF-β receptor II in mouse lung ECs (*Tgfbr2*$^{EC-KO}$) and examined the emergence of miCAPs after bronchial ligation (**Fig. 5d**)[31]. Attenuation of TGF-β signaling transduction inhibited the emergence of miCAPs, shown by both flow cytometry and tissue immunostaining (**Fig. 5e-f and Extended Data Fig. 10b**), indicating that the development of miCAP state requires intact TGF-β signaling activity in CAPs.

TGF-β signaling requires cell surface integrin heterodimers to sequester the latency-associated peptide (LAP) in the latent TGF-β complex, releasing activated TGF-β ligands into the extracellular matrix (ECM) for binding to cognate receptors[29,30,32]. We analyzed the level of integrin genes in AT1 cells using our scRNA-seq data and noted that the expression of both *Itgav* and *Itgb6* were increased in *Cdc42*^{KO} lungs (**Fig. 5g**). Importantly, *Itgb6* is highly expressed in AT1 cells in the mouse and human lung and to a lower level in AT2 cells (**Extended Data Fig. 11a-b**). Immunoblotting using protein from FACS-isolated AT1 cells from control and *Cdc42*$^{AT1-KO}$ mouse lungs confirmed the increased Itgav and Itgb6 protein levels in these cells upon *Cdc42*^{KO} (**Fig. 5h and Extended Data Fig. 10a**). We then determined whether these integrins are responsible for AT1-endothelial mechanotransduction using a small molecule specifically inhibiting Itgb6 heterodimer and its resultant TGF-β activation (Itgb6i)[33]. Compared to vehicle control, the administration of Itgb6i significantly inhibited miCAP emergence in *Cdc42*$^{AT1-KO}$ mouse lungs shown by both flow cytometry and immunostaining (**Fig. 5i-j**). These results together reveal that AT1 cells require Itgb6 integrin-mediated signaling for mechanical signal transmission to their neighboring endothelial cells (**Fig. 5k**).

AT1 mechanosensing can distinguish human lung disease phenotypes

262 Many lung diseases are characterized by aberrant lung mechanics, which contributes to abnormal
263 respiratory function[3]. Fibrotic lung diseases, such as idiopathic pulmonary fibrosis (IPF), exhibit
264 increased tissue stiffness that leads to loss of alveolar capacity[3,34]. By contrast, obstructive lung
265 diseases, including chronic obstructive pulmonary disease (COPD), exhibit an emphysematous
266 phenotype resulting in hyperinflated and degenerated alveoli[3,35]. Using scRNAseq datasets from
267 human disease lungs, we generated a mechanosignaling gene expression score using same
268 YAP/TAZ target genes as described above to evaluate the mechanical activity of cells within the
269 alveoli (**Fig. 6a and Extended Data Fig. 12a**)[24,36]. Compared to other cells, AT1 cells showed
270 significant baseline mechanosignaling activity in healthy human lungs, consistent with our mouse
271 data (**Fig. 2b, 6a and Extended Data Fig. 12a**). Notably, AT1 mechanotransduction was
272 increased in COPD lungs but decreased in IPF (**Fig. 6a and Extended Data Fig. 12a**). In addition,
273 we analyzed our recent scRNAseq data from influenza infected mouse lungs and noted a
274 significant decrease in AT1 mechanotransduction in response to influenza lung injury using our
275 mechanoscore (**Extended Data Fig. 12b**)[17]**.** These findings suggest that AT1 cells are sensitive
276 to both acute viral injury and chronic disease associated changes in lung mechanics.
277
278 We further determined the communication between AT1 cells and their niche neighbors by
279 CellChat analysis using human disease scRNAseq data[36]. AT1 cells showed a significant
280 interaction with their niche neighbors in healthy lungs (**Fig. 6b**). However, in both human COPD
281 and IPF lungs, AT1-driven intercellular communication was greatly reduced, indicating that AT1
282 cells may require an appropriate level of mechanical load to maintain crosstalk with adjacent cells
283 (**Fig. 6b**). Interestingly, expression of mechanosignaling target genes showed distinct disease-
284 associated patterns (**Fig. 6c**). Expression of a subset of genes, such as *RBMS3* and *PTPN14,*
285 were dramatically downregulated in AT1 cells from IPF samples (**Fig. 6c-e**). Other
286 mechanosignaling genes including *CCN1* and *CCN2* were remarkably increased in AT1 cells from
287 COPD lungs, whereas these genes showed minimal changes in those from IPF (**Fig. 6c, f-g**).
288 These results suggest that AT1 cells rely on different transcriptional programs to mediate their
289 mechanosensing in fibrotic versus emphysematous diseases. Taken together, our findings
290 highlight that AT1 cells are a hub of alveolar mechanotransduction, propagating mechanical cues
291 during respiratory movements to maintain overall homeostasis of the lung alveolar niche.
292
293 **Discussion**
294 Biophysical forces impact cell and tissue behaviors in organs such as the lungs. However, which
295 cells are sensitive across the various regions of the lung and how such forces are interpreted and

296 propagated is not understood. Leveraging a reversible bronchial ligation model, we have now
297 demonstrated that respiration-mediated mechanical forces are essential for maintaining multi-
298 cellular homeostasis in the lung alveolus. These studies show that the AT1 lineage is a hub of
299 mechanical signaling in the alveolus, with AT1-specific blockade of mechanotransduction
300 transcriptionally altering neighboring cell lineages including CAPs. The AT1 mechanosensing-
301 induced changes in CAPs are significant and persistent, and are driven in part through
302 integrin/TGF-β signaling resulting from aberrant AT1 mechanosignaling. Mechanotransduction
303 also occurs in human AT1 cells and is altered in disease, and these changes can phenotypically
304 distinguish fibrotic versus emphysematous diseases. Thus, our study defines the niche-
305 dependent role for mechanotransduction in the lung alveolus and reveals that changes in specific
306 cell behavior and response are altered in chronic human lung diseases.
307
308 Aberrant lung mechanics is a hallmark of various human lung diseases[3]. Chronic lung diseases
309 such as COPD and IPF are characterized by alterations in tissue elasticity and stiffness,
310 respectively[34,35]. In addition, in human patients, forced ventilation of the lungs in acute diseases
311 such as acute respiratory distress syndrome (ARDS) can lead to severe lung damage due to
312 changes in mechanical load[37]. The bronchial ligation model may lead to a better understanding
313 of mechanisms driven by deregulated lung mechaosignaling and provide insights on how aberrant
314 mechanics impact lung tissue structure and function in lung diseases. While genetic models of
315 mechanotransduction have led to important discoveries in lung homeostasis and function, most
316 of these models represent irreversible modulation in mechanotransduction and thus cannot be
317 utilized to assess the alterations that occur upon resolution of such inhibitory impulses[4,8,25]. The
318 development of the reversible bronchial ligation model has allowed us to study cellular changes
319 in response to release of lung motion blockade. The changes in cell transcriptome and state we
320 have observed suggest that even if lung motion and tissue architecture can be normalized,
321 persistent changes in cell state and behavior can occur, which may further impact tissue
322 responses to therapeutic interventions and subsequent insults and injuries. Moreover, clinical
323 treatments of various lung diseases involve interventions in lung mechanical load, such as
324 mechanical ventilation[38]. The reversible bronchial ligation model may also help understand
325 whether and how such temporarily altered lung mechanics may impact tissue structure and
326 function in the long term.
327
328 Altered mechanosignaling in AT1 cells impacts the fate of multiple neighboring cell types including
329 endothelial cells. Blocking AT1 cell mechanotransduction induces a *Ntrk2*$^{+}$/*CD74*$^{+}$ CAP state

330 (miCAP) that is also observed in our bronchial ligation model. Previous work has also revealed a
331 transcriptionally similar endothelial cell state that emerges after acute viral lung injuries and
332 chronic lung fibrosis[17,19,39,40]. suggesting the existence of miCAPs may arise from dysfunctional
333 AT1 mechanosensing during both acute and chronic diseases states. Compared to *Ntrk2*-
334 negative CAPs, miCAPs spontaneously respond to normalization of respiration-mediated
335 mechanical forces in our reversible bronchial ligation model by re-entering the cell cycle and
336 differentiating into CAP2s, indicating these cells can act as a potential progenitor during
337 endothelial regeneration after mechanical insults.
338
339 How mechanical forces are propagated between cells within a tissue niche has remained poorly
340 understood due to the complexities of studying multi-cellular biophysical force changes *in vivo*.
341 The induction of the miCAP state upon loss of mechanical signaling in AT1 cells is dependent on
342 endothelial TGF-β signaling induced by the AT1-specific integrin Itgb6. Multiple studies have
343 implicated integrin signaling including that by Itgb6 heterodimers in fibrotic diseases such as IPF.
344 This has led to the development of therapeutic strategies to treat lung fibrosis through inhibition
345 of integrins that blocks the resultant activation of TGF-β ligands[32,41-45]. This approach is validated
346 by our findings that Itgb6 blockade using a small molecule dramatically inhibited CAP phenotypic
347 changes driven by TGF-β signaling activation. Since *Itgb6* expression is restricted to AT1 cells in
348 both the mouse and human lung, blocking its function could have deleterious effects on certain
349 AT1-dependent lung function. Thus, while pharmacological Itgb6 inhibition can efficiently reduce
350 TGF-β-dependent tissue stiffening, it may also disrupt AT1 mechanosensing-mediated tissue
351 homeostasis and regeneration, leading to unexpected side effects. Therefore, a detailed
352 characterization of integrin function in distinct cell types may need to be revisited as these
353 therapies are developed for IPF and other diseases.
354
355 Lung diseases span a range of phenotypic changes in tissue architecture from pulmonary fibrosis
356 which is characterized by increased extracellular matrix (ECM) deposition and stiffing of lung
357 tissue, to emphysematous diseases such as COPD which are marked by loss of alveolar structure
358 and impaired tissue elasticity[3,34,35]. Our analysis reveals aberrant mechanotransduction in human
359 AT1 cells in both IPF and COPD lungs, suggesting AT1 mechanotransduction is sensitive to
360 abnormal tissue compliance. Whether and how AT1 mechanosensing-mediated cell responses
361 play a role in the onset and progression of these diseases requires further investigation.
362 Mechanotransduction in AT1 cells maintains the integrity of ECM through TGF-β signaling and
363 may act as a potential mechanism underlying compromised ECM deposition and function during

progressive pulmonary fibrosis and emphysema[28]. Furthermore, AT1 mechanosignaling-driven gene transcription is distinct between IPF and COPD, suggesting that specific transcription program may direct tissue towards fibrotic or emphysematous responses.

Taken together, our studies highlight that AT1 cells propagate biophysical signals induced by respiratory movements to maintain overall lung homeostasis. Dysregulated AT1 mechanosensing leads to significant changes in fate and behavior of alveolar cells that are essential for lung structure and function. In addition, AT1 mechanosensing is altered in both acute and chronic lung diseases and can help phenotypically differentiate between fibrotic versus emphysematous diseases. Future studies characterizing mechanosensing-induced tissue responses in complex organs such as the lung will be critical to understand the mechanisms underlying onset and progression of various diseases and could provide directions for the development of new therapeutics.

References

1 Weibel, E. R. Lung morphometry: the link between structure and function. *Cell Tissue Res* **367**, 413-426 (2017). https://doi.org:10.1007/s00441-016-2541-4

2 Zepp, J. A. & Morrisey, E. E. Cellular crosstalk in the development and regeneration of the respiratory system. *Nat Rev Mol Cell Biol* **20**, 551-566 (2019). https://doi.org:10.1038/s41580-019-0141-3

3 Pride, N. B. & Macklem, P. T. in *Comprehensive Physiology* 659-692.

4 Shiraishi, K. *et al.* Biophysical forces mediated by respiration maintain lung alveolar epithelial cell fate. *Cell* **186**, 1478-1492 e1415 (2023). https://doi.org:10.1016/j.cell.2023.02.010

5 Wu, H. *et al.* Progressive Pulmonary Fibrosis Is Caused by Elevated Mechanical Tension on Alveolar Stem Cells. *Cell* **180**, 107-121 e117 (2020). https://doi.org:10.1016/j.cell.2019.11.027

6 Li, J. *et al.* The Strength of Mechanical Forces Determines the Differentiation of Alveolar Epithelial Cells. *Dev Cell* **44**, 297-312 e295 (2018). https://doi.org:10.1016/j.devcel.2018.01.008

7 Ahmed, D. W. *et al.* Local photocrosslinking of native tissue matrix regulates lung epithelial cell mechanosensing and function. *Nat Mater* **24**, 1812-1825 (2025). https://doi.org:10.1038/s41563-025-02329-0

8 Penkala, I. J. *et al.* Age-dependent alveolar epithelial plasticity orchestrates lung homeostasis and regeneration. *Cell Stem Cell* **28**, 1775-1789 e1775 (2021). https://doi.org:10.1016/j.stem.2021.04.026

9 Adamson, I. Y. R. & Bowden, D. H. The type 2 cell as progenitor of alveolar epithelial regeneration: A cytodynamic study in mice after exposure to oxygen. *Laboratory Investigation* **30**, 35-42 (1974).

10 Barkauskas, C. E. *et al.* Type 2 alveolar cells are stem cells in adult lung. *J Clin Invest* **123**, 3025-3036 (2013). https://doi.org:10.1172/JCI68782

11 Zacharias, W. J. *et al.* Regeneration of the lung alveolus by an evolutionarily conserved epithelial progenitor. *Nature* **555**, 251-255 (2018). https://doi.org:10.1038/nature25786

12 Liberti, D. C. *et al.* Alveolar epithelial cell fate is maintained in a spatially restricted manner to promote lung regeneration after acute injury. *Cell Rep* **35**, 109092 (2021). https://doi.org:10.1016/j.celrep.2021.109092

13 Strunz, M. *et al.* Alveolar regeneration through a Krt8+ transitional stem cell state that persists in human lung fibrosis. *Nat Commun* **11**, 3559 (2020). https://doi.org:10.1038/s41467-020-17358-3

14 Aros, C. J., Pantoja, C. J. & Gomperts, B. N. Wnt signaling in lung development, regeneration, and disease progression. *Commun Biol* **4**, 601 (2021). https://doi.org:10.1038/s42003-021-02118-w

15 Gillich, A. *et al.* Capillary cell-type specialization in the alveolus. *Nature* **586**, 785-789 (2020). https://doi.org:10.1038/s41586-020-2822-7

16 Niethamer, T. K. *et al.* Defining the role of pulmonary endothelial cell heterogeneity in the response to acute lung injury. *Elife* **9** (2020). https://doi.org:10.7554/eLife.53072

17 Niethamer, T. K. *et al.* Longitudinal single-cell profiles of lung regeneration after viral infection reveal persistent injury-associated cell states. *Cell Stem Cell* **32**, 302-321 e306 (2025). https://doi.org:10.1016/j.stem.2024.12.002

18 Zhao, G. *et al.* Regeneration of the pulmonary vascular endothelium after viral pneumonia requires COUP-TF2. *Sci Adv* **6** (2020). https://doi.org:10.1126/sciadv.abc4493

19 Zhao, G. *et al.* Vascular endothelial-derived SPARCL1 exacerbates viral pneumonia through pro-inflammatory macrophage activation. *Nat Commun* **15**, 4235 (2024). https://doi.org:10.1038/s41467-024-48589-3

20 Zhao, G. *et al.* TGF-betaR2 signaling coordinates pulmonary vascular repair after viral injury in mice and human tissue. *Sci Transl Med* **16**, eadg6229 (2024). https://doi.org:10.1126/scitranslmed.adg6229

21 Ma, S., Meng, Z., Chen, R. & Guan, K. L. The Hippo Pathway: Biology and Pathophysiology. *Annu Rev Biochem* **88**, 577-604 (2019). https://doi.org:10.1146/annurev-biochem-013118-111829

22 Dobrokhotov, O., Samsonov, M., Sokabe, M. & Hirata, H. Mechanoregulation and pathology of YAP/TAZ via Hippo and non-Hippo mechanisms. *Clin Transl Med* **7**, 23 (2018). https://doi.org:10.1186/s40169-018-0202-9

23 Dupont, S. *et al.* Role of YAP/TAZ in mechanotransduction. *Nature* **474**, 179-183 (2011). https://doi.org:10.1038/nature10137

24 Wang, Y. *et al.* Comprehensive Molecular Characterization of the Hippo Signaling Pathway in Cancer. *Cell Rep* **25**, 1304-1317 e1305 (2018). https://doi.org:10.1016/j.celrep.2018.10.001

25 Liu, F. *et al.* Mechanosignaling through YAP and TAZ drives fibroblast activation and fibrosis. *Am J Physiol Lung Cell Mol Physiol* **308**, L344-357 (2015). https://doi.org:10.1152/ajplung.00300.2014

26 Tschumperlin, D. J., Ligresti, G., Hilscher, M. B. & Shah, V. H. Mechanosensing and fibrosis. *J Clin Invest* **128**, 74-84 (2018). https://doi.org:10.1172/JCI93561

27 Zepp, J. A. *et al.* Genomic, epigenomic, and biophysical cues controlling the emergence of the lung alveolus. *Science* **371** (2021). https://doi.org:10.1126/science.abc3172

28 Callaway, D. A. *et al.* TGF-beta controls alveolar type 1 epithelial cell plasticity and alveolar matrisome gene transcription in mice. *J Clin Invest* **134** (2024). https://doi.org:10.1172/JCI172095

29 Massague, J. & Sheppard, D. TGF-beta signaling in health and disease. *Cell* **186**, 4007-4037 (2023). https://doi.org:10.1016/j.cell.2023.07.036

30 Massague, J. TGFbeta signalling in context. *Nat Rev Mol Cell Biol* **13**, 616-630 (2012). https://doi.org:10.1038/nrm3434

31 Liu, B. *et al.* TMEM100, a Lung-Specific Endothelium Gene. *Arterioscler Thromb Vasc Biol* **42**, 1495-1497 (2022). https://doi.org:10.1161/ATVBAHA.122.317683

32 Munger, J. S. *et al.* The integrin alpha v beta 6 binds and activates latent TGF beta 1: a mechanism for regulating pulmonary inflammation and fibrosis. *Cell* **96**, 319-328 (1999). https://doi.org:10.1016/s0092-8674(00)80545-0

33 Patsenker, E. *et al.* Inhibition of integrin alphavbeta6 on cholangiocytes blocks transforming growth factor-beta activation and retards biliary fibrosis progression. *Gastroenterology* **135**, 660-670 (2008). https://doi.org:10.1053/j.gastro.2008.04.009

34 Wijsenbeek, M. & Cottin, V. Spectrum of Fibrotic Lung Diseases. *N Engl J Med* **383**, 958-968 (2020). https://doi.org:10.1056/NEJMra2005230

35 Christenson, S. A., Smith, B. M., Bafadhel, M. & Putcha, N. Chronic obstructive pulmonary disease. *Lancet* **399**, 2227-2242 (2022). https://doi.org:10.1016/S0140-6736(22)00470-6

36 Jones, D. L. *et al.* An injury-induced mesenchymal-epithelial cell niche coordinates regenerative responses in the lung. *Science* **386**, eado5561 (2024). https://doi.org:10.1126/science.ado5561

37 Bos, L. D. J. & Ware, L. B. Acute respiratory distress syndrome: causes, pathophysiology, and phenotypes. *Lancet* **400**, 1145-1156 (2022). https://doi.org:10.1016/S0140-6736(22)01485-4

38 Walter, K. Mechanical Ventilation. *JAMA* **326**, 1452 (2021). https://doi.org:10.1001/jama.2021.13084

39 Kong, C. S. L., V, M., Pantaleon-Garcia, J., Evans, S. E. & Chen, J. Truncated NTRK2 is induced in CAP1 endothelial cells during mouse lung injury-repair. *iScience* **28**, 112973 (2025). https://doi.org:10.1016/j.isci.2025.112973

40 Raslan, A. A. *et al.* Lung injury-induced activated endothelial cell states persist in aging-associated progressive fibrosis. *Nat Commun* **15**, 5449 (2024). https://doi.org:10.1038/s41467-024-49545-x

41 Reed, N. I. *et al.* The alphavbeta1 integrin plays a critical in vivo role in tissue fibrosis. *Sci Transl Med* **7**, 288ra279 (2015). https://doi.org:10.1126/scitranslmed.aaa5094

42 Koth, L. L. *et al.* Integrin beta6 mediates phospholipid and collectin homeostasis by activation of latent TGF-beta1. *Am J Respir Cell Mol Biol* **37**, 651-659 (2007). https://doi.org:10.1165/rcmb.2006-0428OC

43 Roy, A. *et al.* De novo design of highly selective miniprotein inhibitors of integrins alphavbeta6 and alphavbeta8. *Nat Commun* **14**, 5660 (2023). https://doi.org:10.1038/s41467-023-41272-z

44 Horan, G. S. *et al.* Partial inhibition of integrin alpha(v)beta6 prevents pulmonary fibrosis without exacerbating inflammation. *Am J Respir Crit Care Med* **177**, 56-65 (2008). https://doi.org:10.1164/rccm.200706-805OC

45 Madala, S. K. *et al.* Inhibition of the alphavbeta6 integrin leads to limited alteration of TGF-alpha-induced pulmonary fibrosis. *Am J Physiol Lung Cell Mol Physiol* **306**, L726-735 (2014). https://doi.org:10.1152/ajplung.00357.2013

Figure legends

Figure 1: Respiration-mediated mechanical forces maintain multi-cellular homeostasis of the lung alveolus.

a. A schematic of reversible bronchial ligation model that modulates unilateral lung motion. **b.** A schematic of scRNA seq experiment. Cells from wildtype CD1 mouse lungs after sham, bronchial ligation or reversed surgery were isolated and used for scRNA seq analyses. **c.** A merged UMAP plot of distal lung cells from sham, ligated and reversed mouse lungs. Cells were annotated by cell type. **d-f.** UMAP plots of cells from indicated lineages annotated by cell type and treatment.

505 **g.** Percentage of AT1 and AT2 cells in indicated mouse lungs (n = 4 or 5, mean ± S.E.M.). Asterisks
506 indicate statistical significance (** *p* value < 0.01, unpaired two-tailed Student's *t* test). **h.**
507 Percentage of EdU incorporated endothelial cells in indicated mouse lungs (n = 5 or 6, mean ±
508 S.E.M.). Asterisks indicate statistical significance (* *p* value < 0.05, ** *p* value < 0.01, unpaired
509 two-tailed Student's *t* test). NS: no statistical significance. **i.** A model depicting mechanical force-
510 induced cell responses in the lung alveolus.
511
512 **Figure 2: Alveolar cell responses to mechanical forces can be independent of intrinsic**
513 **mechanosignaling.**
514 **a.** A schematic of the YAP/TAZ mechanosignaling pathway. 22 YAP/TAZ target genes reported in
515 Wang et al. 2018 were used to generate cell mechanoscore. **b.** A UMAP plot of distal lung cells
516 from sham mouse lungs. Cells were annotated by cell type. **c-d.** Baseline mechanoscore of each
517 cell type in the distal lung. Red dashed line in (**d**) indicates the mean of mechanoscore across all
518 cells. **e,g.** Euclidian distance indicating cellular transcriptional similarity across treatments. An
519 asterisk indicates statistical significance (* *p* value < 0.05, pairwise Wilcoxon test). NS: no
520 statistical significance. **f,h.** Mechanoscore of indicated cell types in sham, ligation, or reversed
521 mouse lungs. An asterisk indicates statistical significance (* *p* value < 0.05, pairwise Wilcoxon
522 test). NS: no statistical significance.
523
524 **Figure 3: AT1 cells are a mechanotransduction node in the lung.**
525 **a.** A schematic of genetic attenuation of mechanotransduction in AT1s. Control AT1-trace mice or
526 those with a *Cdc42*$^{fl/fl}$ allele were administrated with three doses of tamoxifen, followed by
527 tamoxifen diet. Cells from control or *Cdc42*$^{AT1\text{-}KO}$ mouse lungs were isolated and used for scRNA
528 seq analyses at indicated time points. **b.** A merged UMAP plot of distal lung cells from control or
529 *Cdc42*$^{AT1\text{-}KO}$ mouse lungs. Cells were annotated by cell type. **c-e.** Euclidian distance indicating
530 cellular transcriptional similarity across treatments. Asterisks indicate statistical significance (* *p*
531 value < 0.05, pairwise Wilcoxon test). NS: no statistical significance. **f.** UMAP plots of CAPs from
532 control and *Cdc42*$^{AT1\text{-}KO}$ mouse lungs. Cells were annotated by cell type or treatment. **g.** A dot plot
533 showing expression of indicated genes in each cell type. **h.** Flow cytometry results showing the
534 percentage of AT1-induced CAP in *Cdc42*$^{AT1\text{-}KO}$ mouse lungs after three doses of tamoxifen for 14
535 or 28 days, or control mouse lungs (n = 5, mean ± S.E.M.). Asterisks indicate statistical
536 significance (** *p* value < 0.01, **** *p* value < 0.0001, unpaired two-tailed Student's *t* test). **i.**
537 Representative IHC images of control or *Cdc42*$^{AT1\text{-}KO}$ mouse lungs stained with TrkB and ERG

538 (scale bar = 25 μm). **j.** A model depicting AT1 cells as a node of mechanotransduction in the
539 alveolus.
540
541 **Figure 4: The AT1 mechanosensing-induced CAP state is permanent and functionally**
542 **distinct.**
543 **a.** UMAP plots of CAPs from sham, ligated and reversed mouse lungs. Cells were annotated by
544 cell type or treatment. **b.** A bar plot showing percentage of each cell type in sham, ligated or
545 reversed mouse lungs. **c.** A feature plot showing *Ntrk2* expression in ligation-induced CAPs. **d.** A
546 Spearman correlation showing transcriptional similarity between AT1-induced CAPs and ligation-
547 induced CAPs. **e.** Flow cytometry results showing miCAP percentage in indicated lung tissues (n
548 = 5 or 6, mean ± S.E.M.). Asterisks indicate statistical significance (* p value < 0.05, *** p value <
549 0.001, unpaired two-tailed Student's t test). NS: no statistical significance. **f.** Representative IHC
550 images of indicated lung tissues stained with TrkB and ERG, a pan endothelial cell marker (scale
551 bar = 25 μm). **g.** A schematic of miCAP lineage trace experiment. miCAP-trace mice underwent
552 ligation surgery, received three doses of tamoxifen, followed by reversed procedure to restore
553 respiratory motion. Tissues from ligated or reversed miCAP-trace mouse lungs were used for
554 histology. **h.** Representative IHC images of indicated lung tissues stained with the lineage trace
555 marker (tdTomato), a CAP2 marker (CA4), and ERG (scale bar = 50 μm). **i.** Percentage of $CA4^+$
556 miCAP-trace endothelial cells in indicated tissues (n = 3 or 6, mean ± S.E.M.). Asterisks indicate
557 statistical significance (** p value < 0.01, unpaired two-tailed Student's t test). **j.** A schematic of
558 CAP lineage trace experiment. CAP1- or CAP2-trace mice were administrated with one dose of
559 tamoxifen, followed by sham or bronchial ligation surgery. Cells and tissues from control or ligated
560 lung were used for flow cytometry or histology, respectively. **k.** Flow cytometry results showing
561 miCAP percentage in indicated lung tissues (n = 3 or 4, mean ± S.E.M.). Asterisks indicate
562 statistical significance (* p value < 0.05, unpaired two-tailed Student's t test). **l.** Representative
563 IHC images of CAP1- (left) or CAP2-trace (right) mouse lungs after bronchial ligation stained with
564 the lineage trace marker (tdTomato), TrkB, and ERG (scale bar = 100 μm). **m.** A schematic of
565 genetic attenuation of mechanotransduction in CAPs. Control CAP-trace mice or those with a
566 *Cdc42*$^{fl/fl}$ allele were administrated with three doses of tamoxifen. Cells from control or *Cdc42*$^{CAP-}$
567 ^{KO} lung were used for flow cytometry. **n.** Flow cytometry results showing miCAP percentage in
568 indicated lung tissues (n = 4 or 5, mean ± S.E.M.). NS: no statistical significance. **o.** A model
569 depicting miCAP cell origin and fate change in response to mechanical forces.
570

571 **Figure 5: AT1-endothelial mechanotransduction requires integrin/TGF-β signaling.**
572 **a.** A pathway enrichment analysis of CAPs from control and *Cdc42*$^{AT1-KO}$ (D14 and D28) mouse
573 lungs. **b.** An immunoblot showing phosphorylation of SMADs in endothelial cells from control and
574 *Cdc42*$^{AT1-KO}$ (D14) mouse lungs. Three independent mice were included in each group. **c.**
575 Quantification of p-SMAD level relative to total SMAD from immunoblots in (**b**) (n = 3, mean ±
576 S.E.M.). An asterisk indicates statistical significance (* *p* value < 0.05, unpaired two-tailed
577 Student's *t* test). NS: no statistical significance. **d.** A schematic of genetic attenuation of TGF-β
578 signaling in endothelial cells. Control EC-trace mice or those with a *Tgfbr2*$^{fl/fl}$ allele were
579 administrated with three doses of tamoxifen, followed by ligation surgery after 7 days. Cells and
580 tissues from ligated control or *Tgfbr2*$^{EC-KO}$ mouse lungs were used for flow cytometry or histology,
581 respectively. **e.** Flow cytometry results showing miCAP percentage in indicated lung tissues (n =
582 3 or 5, mean ± S.E.M.). An asterisk indicates statistical significance (* *p* value < 0.05, unpaired
583 two-tailed Student's *t* test). **f.** Representative IHC images of indicated lung tissues stained with
584 TrkB and ERG, a pan endothelial cell marker (scale bar = 25 μm). **g.** A dot plot showing indicated
585 *Integrin* expression in AT1 cells from control and *Cdc42*$^{AT1-KO}$ mouse lungs. Red dashed boxes
586 indicate specific *Integrin* with increased expression after *Cdc42*$^{AT1-KO}$. **h.** An immunoblot showing
587 increased level of Itgav and Itgb6 in AT1 cells from control and *Cdc42*$^{AT1-KO}$ mouse lungs. AT1
588 cells from three independent mice were pooled and used for protein extraction in each group. **i.**
589 Representative IHC images of lung tissues from *Cdc42*$^{AT1-KO}$ mice in the presence of vehicle or a
590 small-molecule Itgb6 inhibitor administration (scale bar = 25 μm). **j.** Flow cytometry results
591 showing miCAP percentage in indicated lung tissues (n = 4 or 5, mean ± S.E.M.). Asterisks
592 indicate statistical significance (** *p* value < 0.01, unpaired two-tailed Student's *t* test). **k.** A model
593 depicting integrin/ TGF-β-dependent crosstalk between AT1 cells and CAPs.
594
595 **Figure 6: The AT1-driven mechanosensing network is altered in human lung disease.**
596 **a.** Mechanoscore of indicated cells from human healthy, COPD, and IPF lung tissues generated
597 using pseudobulk aggregated expression of YAP/TAZ target genes described above in Fig. 2a
598 (median ± S.D.). An asterisk indicates statistical significance (* *p* value < 0.05, Kruskal-Wallis test
599 followed by Dunn test). **b.** CellChat analysis showing communication strength between indicated
600 cell types from human healthy, COPD, and IPF lung tissues. **c.** A heatmap showing expression of
601 YAP/TAZ target genes used for mechanoscore in AT1 cells from human healthy, COPD, and IPF
602 lung tissues. **d-g.** Pseudobulk aggregated expression of indicated genes in AT1 cells from human

603 healthy, COPD, and IPF lungs (median ± S.D.). An asterisk indicates statistical significance (* *p*
604 value < 0.05, Kruskal-Wallis test followed by Dunn test).
605
606 **Methods**
607 *Human subjects*
608 All human samples used in this study were obtained following an established protocol
609 (Prospective Registry of Outcomes in Patients Electing Lung Transplantation (PROPEL))
610 approved by University of Pennsylvania Institutional Review Board, as previously reported[36].
611 Informed consent was performed in accordance with institutional and NIH procedures. The
612 institutional review board of the University of Pennsylvania approved this study, and all patient
613 information was deidentified before use.
614
615 *Mouse studies*
616 All mouse experiments were performed following the protocols of the University of Pennsylvania
617 Institutional Animal Care and Use Committee. Adult mice (8-12 weeks old) were used in all the
618 experiments. Cre recombination was initiated by a single dose of tamoxifen (200 mg/kg Sigma-
619 Aldrich) for lineage tracing and 1 dose of tamoxifen (200 mg/kg, Sigma-Aldrich) daily for 3
620 consecutive days for conditional gene knockout, unless otherwise indicated. The small-molecule
621 Itgb6 inhibitor EMD527040 (Tocris Bioscience Cat#7508) was dissolved in 10% DMSO in saline
622 and administrated intraperitoneally at 20 mg/kg every other day.
623
624 Mouse lines used in this study were previously validated and the strains are listed below:

Mouse strain	**Source**	**Catalog#**
CD-1	Charles River	022
[46]*Hopx*^{CreERT2}	Jackson Laboratory	017606
R26R^{EYFP}	Jackson Laboratory	007903
[47]*Cdc42*^{flox}	Jackson Laboratory	027576
[48]*Ntrk2*^{CreERT2}	Jackson Laboratory	027214
[49]*Kit*^{MerCreMer}	Jackson Laboratory	032052
[17]*Car4*^{CreERT2}	Morrisey lab	NA
R26R^{tdTomato}	Jackson Laboratory	007914
[31]*TMEM100*^{CreERT2}	Jackson Laboratory	014159
R26R^{ZsGreen}	Jackson Laboratory	007906

[50]Tgfbr2[flox]	Jackson Laboratory	012603

625

626 *Reversible bronchial ligation*

627 Mice were anesthetized with isoflurane and intubated for ventilation using a MiniVent ventilator
628 (Harvard apparatus; tidal volume of 10 µL per gram mouse body weight, respiratory rate of 150
629 breaths per minute). The thoracic cavity was exposed by incising 1 cm on the left lateral side of
630 the skin, followed by a 0.5 cm incision at the third left intercostal space. The left main bronchus
631 was clipped using a customized micro vascular clamp (Fine Science Tools Cat#00396-01, jaw
632 dimension = 2 x 1 mm) with a micro clamp applying forceps (Fine Science Tools Cat#00071-14).
633 For reversal, mice were anesthetized and intubated following the same protocol. An incision was
634 made at the fourth left intercostal space to expose thoracic cavity, followed by removal of the clip.

635

636 *Micro-computed tomography (uCT)*

637 uCT images were generated using a X-Cube CT scanner (Molecubes) located at the Small Animal
638 Imaging Facility at Penn Medicine. Live mice were anesthetized with isoflurane and images were
639 acquired using a respiratory gating approach. The settings for image acquisition were as follows:
640 reconstructed voxel size: 100 um, X-Ray tube voltage: 50 kVp, X-Ray tube current: 440 uA,
641 exposure time: 32 ms, type of filter used: 0.8 mm aluminum filter, degree of rotation stepping: 0.75
642 degrees (480 total steps in a 360 degree scan).

643

644 *Histology*

645 For tissue preparation, mice were euthanized by CO_2 inhalation and the lungs were perfused with
646 PBS, followed by inflation with 2% Paraformaldehyde (Thermo Fisher Scientific) at a constant
647 pressure of 25 cm H_2O. Tissues were fixed at 4°C overnight and dehydrated in a series of ethanol
648 concentration gradients. After dehydration, tissues were embedded in paraffin and sliced into 6
649 µm thick sections.

650

651 Hematoxylin and eosin (H&E) staining was performed as previously described[17,36]. For
652 immunostaining, the following antibodies were used on paraffin tissue sections:

Antibody	**Source**	**Catalog#**
Goat polyclonal anti-TrkB	Novus Biologicals	AF1494
Mouse monoclonal anti-ERG	Abcam	ab214341
Rabbit monoclonal anti-ERG	Abcam	ab92513

Rabit polyclonal anti-RFP	Rockland	600-401-379
Rat monoclonal anti-LAMP3	Novus Biologicals	DDX0191P-100
Mouse monoclonal anti-HOPX	Santa Cruz	sc-398703
Rabbit monoclonal anti-NKX2.1 (TTF1)	Abcam	ab76013
Goat polyclonal anti-CA4	Novus Biologicals	AF2414

Imaging and image analysis

H&E stained lung sections were tile-scanned at 4x using a Nikon Eclipse Ni series microscope. Fluorescent images were acquired at 20x and 40x using z-stacks on a Zeiss LSM 710 or Leica Stellaris 5 laser scanning confocal microscope. Cell counting analysis was performed using FIJI.

Single cell isolation, flow cytometry, and FACS

Lungs were harvested and digested into single cell suspensions as previously described[17,36]. For single cell dissociation from ligated mouse lungs, lungs were perfused, inflated with PBS, followed by inflation with digestion buffer supplemented with collagenase I, dispase, and DNase I prior to the removal of lobes.

For flow cytometry, cells were stained with combination of antibodies for 30 min on ice before subjected to a flow cytometer. For FACS, lung cells were incubated with mouse CD45 MicroBeads magnetic beads (Miltenyi Biotec Cat#130-052-301) and the $CD45^{+}$ population was depleted as per the manufacturer's protocol. $CD45^{-}$ cells were then incubated with CD31 or/and CD326 antibodies and subjected to FACS for isolation of specific cell populations.

Antibodies used and dilutions are listed below:

Antibody (Dilution)	**Source**	**Catalog#**
CD45-PerCP-Cy5.5 (1:200)	Thermo Fisher	45-0451-82
CD45-PE-Cy7 (1:200)	Thermo Fisher	25-0451-82
CD45-APC-Cy7 (1:200)	BioLegend	103116
CD31-PE-Cy7 (1:200)	Thermo Fisher	25-0311-82
CD31-PE (1:200)	BioLegend	102508
CD326-PE-Cy7 (1:200)	Thermo Fisher	25-5791-80
TrkB-Biotin (1:100)	R&D systems	BAF1494
Streptavidin-APC (1:200)	Thermo Fisher	17-4317-82

673 *EdU proliferation assay*

674 5-Ethynyl-2'-deoxyuridine (Santa Cruz Biotechnology Cat#sc-284628B) was dissolved in tap
675 water at a concentration of 2 g/L, filtered through a 0.2 μm filter, and stored at 4°C. To create a
676 drinking water solution, this stock solution was diluted to a final concentration of 0.2 g/L in tap
677 water and sterile filtered. Mice consumed EdU water over the time course indicated. EdU
678 incorporation was detected using the Click-iT™ Plus EdU Alexa Fluor™ 488 Flow Cytometry
679 Assay Kit (Thermo Fisher #C10632) according to the manufacturer's protocol.

680

681 Immunoblotting alaysis

682 Total protein was extracted from FACS sorted lung endothelial cells or AT1 cells from indicated
683 animals using SDS sample buffer (BioRad) supplemented with 2-Mercaptoethanol (Sigma) and a
684 cocktail of protease and phosphatase inhibitors (Thermo). Samples were boiled for 5 min,
685 followed by SDS polyacrylamide gel electrophoresis. Proteins were then transferred to a
686 nitrocellulose membrane and immunoblotted. Primary and secondary antibodies used are listed
687 as below:

Antibody (Dilution)	**Source**	**Catalog#**
Rabbit monoclonal P-SMAD2/3 (1:1000)	Cell Signaling Technology	8828
Rabbit monoclonal SMAD2/3 (1:1000)	Cell Signaling Technology	8685
Rabbit polycloncal P-SMAD1/5/8 (1:1000)	Millipore Sigma	AB3848-I
Rabbit polycloncal SMAD1/5/8/9 (1:1000)	Abcam	ab13723
Rabbit monoclonal GAPDH (1:1000)	Cell Signaling Technology	8884
Rabbit monoclonal Itgav (1:1000)	Abcam	ab179475
Rabbit monoclonal Itgb6 (1:1000)	Abcam	ab187155
Rabbit monoclonal β-actin (1:1000)	Cell Signaling Technology	4970
Donkey anti-mouse HRP (1:10000)	Jackson Immunoresearch	715-035-150
Donkey anti-rabbit HRP (1:10000)	Jackson Immunoresearch	711-035-152

688

689 *Quantitative RT-PCR*

690 Total RNA was extracted from sorted CAP-trace cells using a RNeasy Mini Kit (Qiagen
691 Cat#74104), reverse transcribed to cDNA using a SuperScriptTM IV kit (Invitrogen
692 Cat#18091050), and used for quantitative PCR reaction on a QuantStudio 7 PCR System
693 (Applied Biosystems) using specific Taqman Probes (Thermo Fisher) or SYBR-Green primers
694 (Integrated DNA Technologies) as listed below:

SYBR-Green primer	Sequence
Cdc42 Forward	5'-GAGAAGCTGAGGACAAGATCTAA-3'
Cdc42 Reverse	5'-CACCATCACCAACAACAACAC-3'
Gapdh Forward	5'-AAATGGTGAAGGTCGGTGTGAACG-3'
Gapdh Reverse	5'-ATCTCCACTTTGCCACTGC-3'
Taqman probe	**Catalog#**
Ccn1	Mm00487498_m1
Ccn2	Mm01192233_g1
Ankrd1	Mm00496512_m1
Gapdh	Mm99999915_g1

695

696 *scRNAseq and analysis*

697 To create samples for scRNAseq that adequately represented both immune and non-immune
698 compartments, we used magnetic activated cell sorting (MACS) to isolate $CD45^+$ and $CD45^-$ cells
699 and recombined them at a ratio of 85% CD45- cells to 15% CD45+ cells. Cells were counted
700 using the Countess II FL Automated Cell Counter (Thermo Fisher) and loaded at a concentration
701 of 800-1000 cells/mL onto a 10X Chromium Next Gem Controller (10X Genomics) following the
702 manufacturer's instructions. cDNA and sequencing libraries were prepared using Chromium Next
703 GEM Single Cell 3' kit v3.1. cDNA and library quality control were performed using an Agilent
704 2100 Bioanalyzer using the Bioanalyzer High Sensitivity DNA kit (Agilent #5067-4626). Libraries
705 were then sequenced on an Illumina Novaseq 6000 instrument.

706

707 Read Alignment, UMI Processing, and Gene Quantification: Raw sequencing data (BCL files)
708 were converted to FASTQ format using bcl2fastq. Reads were aligned to the GRCm39 mouse
709 reference genome using STARsolo (STAR v2.7.11b)[51] for alignment, barcode and UMI correction,
710 and gene-level quantification in single-cell mode. STARsolo was run with 10x Genomics
711 Cellranger chemistry presets and configured to output both exonic gene counts (--soloFeatures
712 GeneFull). Only barcodes classified as valid cells by STARsolo's Emptydrops implementation.

713

714 Ambient RNA Correction: To reduce contamination from ambient RNA generated by lysed cells
715 during tissue dissociation, we applied SoupX (v1.6.0)[52] to each sample independently. For each
716 library, SoupX estimated the proportion of background RNA by identifying expression signatures
717 enriched in empty droplets relative to putative cell-containing droplets. The corrected count matrix
718 was obtained using the adjustCounts() function with sample-specific contamination fractions

estimated via the autoEstCont() workflow. Post-correction matrices were manually inspected to ensure appropriate removal of canonical ambient signals (e.g., mitochondrial transcripts, hemoglobin genes and ribosomal RNAs). Only contamination-adjusted matrices were used for downstream analysis.

Quality Control and Filtering: Cells with fewer than 200 detected genes, cells exceeding three median absolute deviations (MADs) above the gene-count distribution, cells with a log10GenesPerUMI less than 80% and cells with more than 20% mitochondrial RNA content were excluded. Potential doublets were identified using Scrublet and excluded. All remaining cells were retained for downstream analysis. For experiments that included mixed sexes, X- and Y-linked genes were removed from the variable feature set prior to PCA to prevent sex-specific effects from dominating downstream analyses. Non-linear dimensionality reduction was performed using Uniform Manifold Approximation and Projection (UMAP), and Louvain graph-based clustering was applied, both using the top 30 principal components.

Marker genes for each cell type were identified using the FindAllMarkers command using the RNA assay within Seurat. Correlation analysis was performed in R and correlation plots made using ggcorrplot. Gene set enrichment analysis (GSEA) of gene ontology (GO) was performed using the 'clusterProfiler' package (DOI: 10.18129/B9.bioc.clusterProfiler). Mechanoscore gene signatures were obtained from a previously published YAP/TAZ target gene set[24]. Gene signature activity scores were computed using the UCell R package, which implements a rank-based method to quantify gene set enrichment at the single-cell level[53].

Cell–cell communication analysis was performed using CellChat v2, which infers intercellular signaling networks by integrating known ligand–receptor interactions with single-cell transcriptomic data[54]. For this study, CellChat analysis was restricted to a biologically relevant subset of cell types derived from the human disease samples. All analyses were carried out following the standard CellChat workflow, including data preprocessing, identification of overrepresented ligand–receptor pairs, inference of communication probabilities, and visualization of network-level signaling patterns.

To minimize technical and biological variation, we used a pseudobulk framework in which single-cell counts were aggregated at the donor–cell type level. For each annotated cell type, all cells from the same donor were summed to generate a donor-level expression profile. Pseudobulk

753 matrices were constructed using the Seurat2pb function implemented within the edgeR
754 package[55]. Heatmaps were constructed using the Complexheatmap package in R.
755
756 *Statistical analysis*
757 In all mouse experiments, statistical significance was determined by an unpaired two-tailed
758 Student's *t* test between two groups using Graphpad Prism 10. Statistical analysis of scRNA seq
759 data was performed in R. Details of statistical analysis used for each experiment are indicated in
760 the figure legends.
761

762 **Methods references**

763 46 Takeda, N. *et al.* Interconversion between intestinal stem cell populations in distinct
764 niches. *Science* **334**, 1420-1424 (2011). https://doi.org:10.1126/science.1213214
765 47 Chen, L. *et al.* Cdc42 deficiency causes Sonic hedgehog-independent holoprosencephaly.
766 *Proc Natl Acad Sci U S A* **103**, 16520-16525 (2006).
767 https://doi.org:10.1073/pnas.0603533103
768 48 Rutlin, M. *et al.* The cellular and molecular basis of direction selectivity of Adelta-LTMRs.
769 *Cell* **159**, 1640-1651 (2014). https://doi.org:10.1016/j.cell.2014.11.038
770 49 van Berlo, J. H. *et al.* c-kit+ cells minimally contribute cardiomyocytes to the heart. *Nature*
771 **509**, 337-341 (2014). https://doi.org:10.1038/nature13309
772 50 Leveen, P. *et al.* Induced disruption of the transforming growth factor beta type II receptor
773 gene in mice causes a lethal inflammatory disorder that is transplantable. *Blood* **100**, 560-
774 568 (2002). https://doi.org:10.1182/blood.v100.2.560
775 51 Dobin, A. *et al.* STAR: ultrafast universal RNA-seq aligner. *Bioinformatics* **29**, 15-21
776 (2013). https://doi.org:10.1093/bioinformatics/bts635
777 52 Young, M. D. & Behjati, S. SoupX removes ambient RNA contamination from droplet-
778 based single-cell RNA sequencing data. *Gigascience* **9** (2020).
779 https://doi.org:10.1093/gigascience/giaa151
780 53 Feichtinger, X. *et al.* Improved biomechanics in experimental chronic rotator cuff repair
781 after shockwaves is not reflected by bone microarchitecture. *PLoS One* **17**, e0262294
782 (2022). https://doi.org:10.1371/journal.pone.0262294
783 54 Jin, S., Plikus, M. V. & Nie, Q. CellChat for systematic analysis of cell-cell communication
784 from single-cell transcriptomics. *Nat Protoc* **20**, 180-219 (2025).
785 https://doi.org:10.1038/s41596-024-01045-4
786 55 Robinson, M. D., McCarthy, D. J. & Smyth, G. K. edgeR: a Bioconductor package for
787 differential expression analysis of digital gene expression data. *Bioinformatics* **26**, 139-
788 140 (2010). https://doi.org:10.1093/bioinformatics/btp616

789

790 **Acknowledgements**

791 We thank the Flow Cytometry Core Laboratory at the Children's Hospital of Philadelphia, the Cell
792 and Developmental Biology Microscopy Core at the University of Pennsylvania (UPenn), and the
793 Rodent Cardiovascular Phenotyping Core at the Cardiovascular Institute of UPenn, for their
794 technical assistance. This research was supported by the National Institutes of Health
795 (R01HL164929, R01HL152194, R01HL132999, R01HL162683, R01HL168803 to E.E.M.).

796

797 **Author contributions**

798 Conceptualization: C.S. and E.E.M. Methodology: C.S., M.P.M., S.E.S., G.Z., J.D.P., U.V.C.,
799 D.L.J., M.K., Y.Y., S.Z., S.L., H.H., and A.L. Investigation: C.S., M.P.M., S.E.S., G.Z., and J.D.P.
800 Visualization: C.S., M.P.M., J.D.P., and E.E.M. Supervision: M.C.B. and E.E.M. Writing: C.S. and
801 E.E.M.

802

803 **Competing interest**

804 The authors declare no competing interests.

805

806 **Data availability**

807 All newly generated mouse scRNAseq data have been deposited into GEO (GSE310385).

808

809 **Extended data figure legends**

810 **Extended Data Figure 1: Reversed surgery rescues motion blockade from bronchial**
811 **ligation.**

812 **a.** Representative micro-CT scan images showing restored lung inflation after clip removal in
813 mouse ligated lungs. A schematic of experiment is shown in Fig. 1b. **b.** Representative H&E
814 images of indicated mouse lungs. A schematic of experiment is shown in Fig. 1b. **c.** A dot plot
815 showing marker gene expression in each cell type from the reversible bronchial ligation
816 scRNAseq dataset. A schematic of experiment is shown in Fig. 1b and a UMAP is shown in Fig.
817 1c.

818

819 **Extended Data Figure 2: Respiration-mediated mechanical forces control alveolar**
820 **epithelial composition.**

821 **a.** Representative IHC images of indicated lung tissues stained with HOPX (AT1 cell marker),
822 LAMP3 (AT2 cell marker) and NKX2.1 (pan epithelial cell marker) (scale bar = 50 μm). A
823 quantification of AT1/AT2 ratio in each condition is shown in Fig. 1g. **b.** Gene set enrichment
824 analysis results showing altered pathways in AT2 cells from indicated mouse lungs.

825

826 **Extended Data Figure 3: Respiration-mediated mechanical forces control alveolar**
827 **endothelial cell proliferation.**

828 **a.** A schematic of flow cytometry experiment determining proliferation in lung endothelial cells
829 (ECs). EdU water (0.2 g/L) was provided to mice during indicated time periods. Cells from wildtype

830 mouse after sham, ligation or reversed surgery were isolated and used for flow cytometry. **b.**
831 Representative gating strategies of flow cytometry detecting EdU^+ ECs. A quantification of EdU^+
832 ECs in each condition is shown in Fig. 1h. **c.** Gene set enrichment analysis results showing altered
833 pathways in capillary endothelial cells (CAPs) from indicated mouse lungs.
834
835 **Extended Data Figure 4: Respiration-mediated mechanical forces control gene**
836 **transcription in lung cells.**
837 **a.** Mechanoscore of each cell type in the distal lung after sham, ligation or reversed surgery. Red
838 dashed line indicates the mean of mechanoscore across all cells at baseline. **b.** Euclidian distance
839 indicating cellular transcriptional similarity across treatments in indicated cell types.
840
841 **Extended Data Figure 5: Perturbed mechanosignaling in AT1 cells alters gene transcription**
842 **in neiboring cells within the alveolus.**
843 **a.** A dot plot showing marker gene expression in each cell type from the *Cdc42*$^{AT1\text{-}KO}$ scRNA seq
844 dataset. A schematic of experiment is shown in Fig. 3a and a UMAP is shown in Fig. 3b. **b.**
845 Euclidian distance indicating cellular transcriptional similarity across treatments in indicated cell
846 types.
847
848 **Extended Data Figure 6: Perturbed mechanosignaling in AT1 cells induces the emergence**
849 **of $TrkB^+$ CAP state.**
850 **a.** Representative gating strategies of flow cytometry detecting $TrkB^+$ ECs. A quantification of TrkB
851 $^+$ ECs in each condition is shown in Fig. 3h.
852
853 **Extended Data Figure 7: Expression of signature genes in miCAPs.**
854 **a-b.** Feature plots showing expression of miCAP signature genes in CAP subset from (**a**)
855 reversible ligation or (**b**) *Cdc42*$^{AT1\text{-}KO}$ scRNA seq dataset.
856
857 **Extended Data Figure 8: The miCAP state is functionally distinct.**
858 **a-b.** Representative gating strategies of flow cytometry detecting EdU^+ miCAPs. A schematic of
859 experiment is shown in Extended Data Fig. 3a. **c.** Quantification of EdU^+ miCAPs or $TrkB^-$ ECs in
860 each condition (n = 5, mean ± S.E.M.). Asterisks indicate statistical significance (* p value < 0.05,
861 ** p value < 0.01, unpaired two-tailed Student's t test). NS: no statistical significance. **d.** A
862 schematic of miCAP lineage labelling. *Ntrk2*^{CreERT2}*; R26R*^{tdTomato} mice received bronchial ligation
863 surgery, followed by three doses of tamoxifen before euthanasia. Cells and tissues from ligated

mouse lungs were used for flow cytometry and immunostaining, respectively. **e.** Representative IHC images of indicated lung tissues stained with RFP (miCAP lineage trace marker), TrkB, and ERG (scale bar = 25 μm). Yellow arrows indicated miCAP lineage$^+$ ECs that marked by TrkB expression. **f-g.** Representative flow cytometry gating showing (**f**) efficiency and (**g**) specificity of miCAP lineage trace model. **h.** Representative IHC images of indicated lung tissues stained with RFP (miCAP lineage trace marker), TrkB, and ERG (scale bar = 25 μm). Yellow arrows indicated miCAP lineage$^+$ ECs that retained TrkB expression, whereas cyan arrows indicated those that lost TrkB expression. **i.** Quantification showing miCAP-trace ECs that are positive for TrkB expression after ligation or reversed surgery (n = 3 or 6, mean ± S.E.M.). Asterisks indicate statistical significance (**** *p* value < 0.0001, unpaired two-tailed Student's *t* test).

Extended Data Figure 9: miCAP emergence is independent of intrinsic CAP mechanosignaling.

a. Representative gating strategies of TrkB$^+$ CAP1- or CAP-trace ECs after ligation. A schematic of experiment is shown in Fig. 4j and a quantification is shown in Fig. 4k. **b.** Quantitative RT-PCR showing the downregulation of mechanosignaling sensitive genes (*Ccn1*, *Ccn2*, *Ankrd1*) after *Cdc42* knockout in CAP1 or CAP2s (n = 4 or 5, mean ± SEM). *Ankrd1* expression was not detected in CAP1 and CAP2 after ligation (n = 1 from each group). Asterisks indicate statistical significance (* *p* value < 0.05, ** *p* value < 0.01, *** *p* value < 0.001, unpaired two-tailed Student's *t* test). **c.** Representative gating strategy of TrkB$^+$ CAP1- or CAP2-trace ECs after lineage-specific *Cdc42* deletion. A schematic of experiment is shown in Fig. 4m and a quantification is shown in Fig. 4n.

Extended Data Figure 10: Representative FACS and flow cytometry gating strategies.

a. Representative gating strategies to isolate lung ECs and AT1 cells by FACS. **b.** Representative flow cytometry gating of TrkB$^+$ ECs after ligation in control or *Tgfbr2*$^{EC\text{-}KO}$ mouse lungs. A schematic of experiment is shown in Fig. 5d and a quantification is shown in Fig. 5e.

Extended Data Figure 11: Integrin β6 is specifically expressed in AT1 cells.

a-b. UMAP plots showing expression of the gene encoding integrin β6 in wildtype (**a**) mouse or (**b**) human lungs. Data in **a.** was also shown in Fig. 2b.

896 **Extended Data Figure 12: AT1 mechanosignaling is altered in acute lung injury and chronic**
897 **lung diseases.**
898 **a.** Mechanoscore of indicated cell types in the tissue from human healthy, COPD, and IPF lungs
899 (Habermann *et al*. 2020, GSE135893; Adams *et al*. 2020, GSE136831) generated using
900 pseudobulk aggregated expression of YAP/TAZ target genes (median ± S.D.). **b.** Mechanoscore
901 of indicated cell types in control and influenza infected mouse lungs (Niethamer *et al*. 2025,
902 GSE262927). An asterisk indicates statistical significance (* p value < 0.05, pairwise Wilcoxon
903 test).

Figure 1

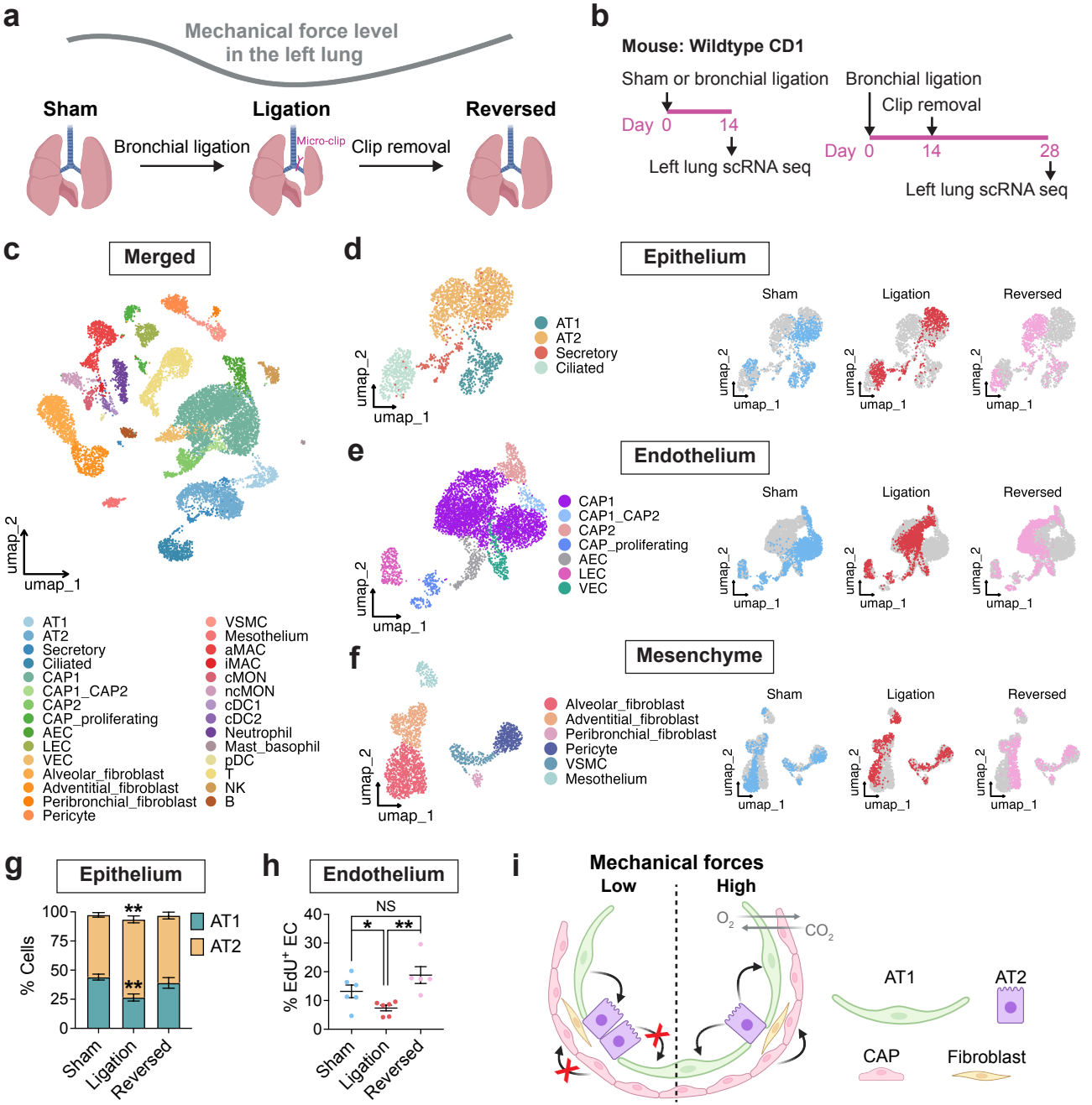
a
Mechanical force level in the left lung
Sham
Ligation
Reversed
Bronchial ligation
Micro-clip
Clip removal
b
Mouse: Wildtype CD1
Sham or bronchial ligation
Day 0
14
Left lung scRNA seq
Bronchial ligation
Clip removal
Day 0
14
28
Left lung scRNA seq
c
Merged
umap_2
umap_1
AT1
AT2
Secretory
Ciliated
CAP1
CAP1_CAP2
CAP2
CAP_proliferating
AEC
LEC
VEC
Alveolar_fibroblast
Adventitial_fibroblast
Peribronchial_fibroblast
Pericyte
VSMC
Mesothelium
aMAC
iMAC
cMON
ncMON
cDC1
cDC2
Neutrophil
Mast_basophil
pDC
T
NK
B
d
Epithelium
Sham
Ligation
Reversed
e
Endothelium
f
Mesenchyme
Alveolar_fibroblast
Adventitial_fibroblast
Peribronchial_fibroblast
Pericyte
VSMC
Mesothelium
g
Epithelium
% Cells
AT1
AT2
Sham
Ligation
Reversed
h
Endothelium
NS
% EdU+ EC
i
Mechanical forces
Low
High
O2
CO2
AT1
AT2
CAP
Fibroblast

Figure 2

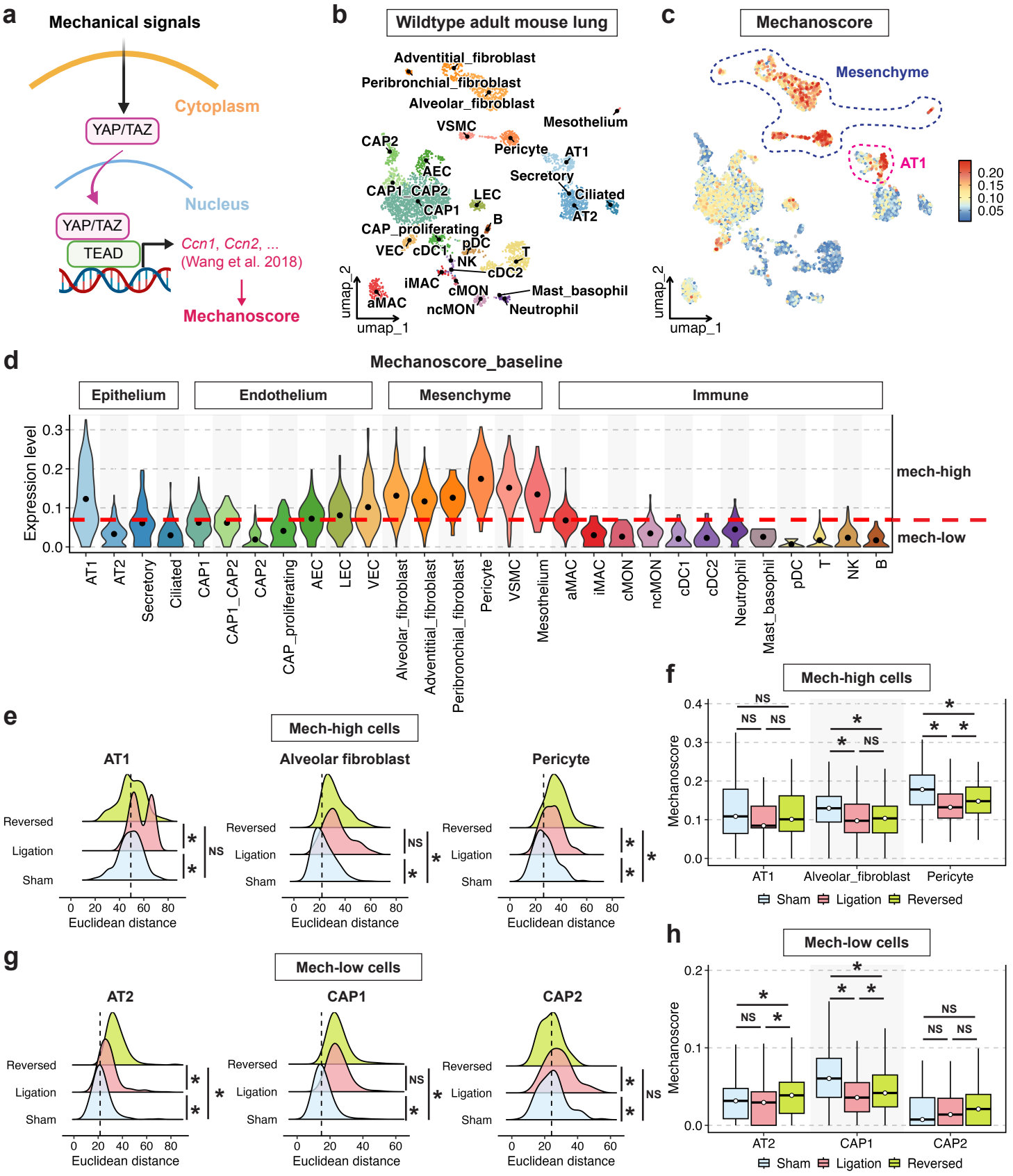
a
Mechanical signals
Cytoplasm
YAP/TAZ
Nucleus
YAP/TAZ
TEAD
Ccn1, Ccn2, ...
(Wang et al. 2018)
Mechanoscore
b
Wildtype adult mouse lung
Adventitial_fibroblast
Peribronchial_fibroblast
Alveolar_fibroblast
Mesothelium
VSMC
CAP2
Pericyte
AT1
AEC
Secretory
CAP1_CAP2
LEC
Ciliated
CAP1
AT2
B
CAP_proliferating
pDC
VEC
cDC1
T
NK
cDC2
iMAC
cMON
Mast_basophil
aMAC
ncMON
Neutrophil
umap_2
umap_1
c
Mechanoscore
Mesenchyme
AT1
0.20
0.15
0.10
0.05
umap_2
umap_1
d
Mechanoscore_baseline
Epithelium
Endothelium
Mesenchyme
Immune
Expression level
0.3
0.2
0.1
0.0
mech-high
mech-low
AT1
AT2
Secretory
Ciliated
CAP1
CAP1_CAP2
CAP2
CAP_proliferating
AEC
LEC
VEC
Alveolar_fibroblast
Adventitial_fibroblast
Peribronchial_fibroblast
Pericyte
VSMC
Mesothelium
aMAC
iMAC
cMON
ncMON
cDC1
cDC2
Neutrophil
Mast_basophil
pDC
T
NK
B
e
Mech-high cells
AT1
Alveolar fibroblast
Pericyte
Reversed
Ligation
Sham
NS
*
0
20
40
60
80
Euclidean distance
f
Mech-high cells
Mechanoscore
0.4
0.3
0.2
0.1
0.0
NS
*
AT1
Alveolar_fibroblast
Pericyte
Sham
Ligation
Reversed
g
Mech-low cells
AT2
CAP1
CAP2
Reversed
Ligation
Sham
NS
*
0
20
40
60
80
Euclidean distance
h
Mech-low cells
Mechanoscore
0.2
0.1
0.0
NS
*
AT2
CAP1
CAP2
Sham
Ligation
Reversed

Figure 3

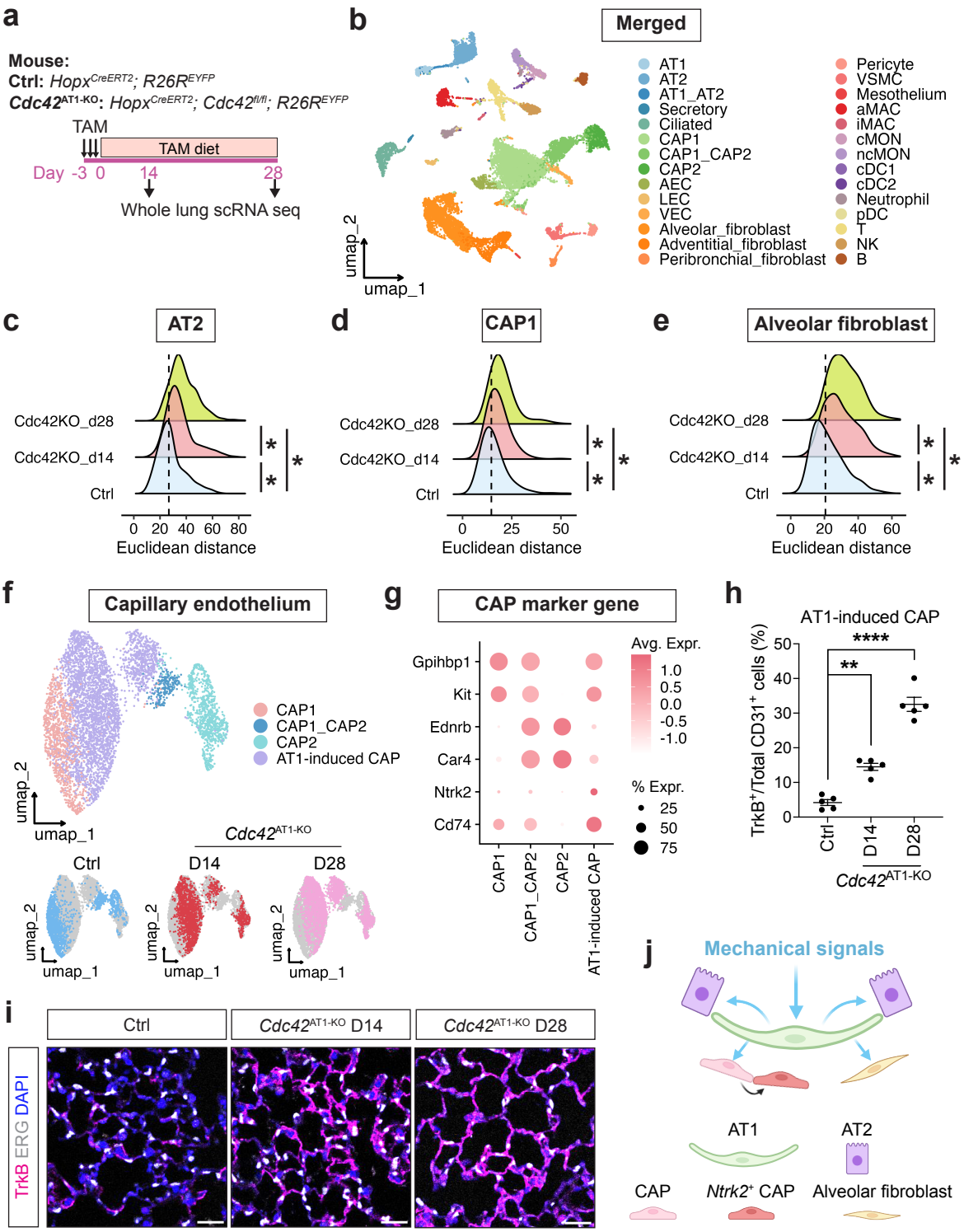
a
Mouse:
Ctrl: Hopx^CreERT2; R26R^EYFP
Cdc42^AT1-KO: Hopx^CreERT2; Cdc42^fl/fl; R26R^EYFP
TAM
TAM diet
Day -3 0 14 28
Whole lung scRNA seq
b
Merged
umap_2
umap_1
AT1
AT2
AT1_AT2
Secretory
Ciliated
CAP1
CAP1_CAP2
CAP2
AEC
LEC
VEC
Alveolar_fibroblast
Adventitial_fibroblast
Peribronchial_fibroblast
Pericyte
VSMC
Mesothelium
aMAC
iMAC
cMON
ncMON
cDC1
cDC2
Neutrophil
pDC
T
NK
B
c
AT2
Cdc42KO_d28
Cdc42KO_d14
Ctrl
Euclidean distance
d
CAP1
Euclidean distance
e
Alveolar fibroblast
Euclidean distance
f
Capillary endothelium
CAP1
CAP1_CAP2
CAP2
AT1-induced CAP
umap_2
umap_1
Cdc42^AT1-KO
Ctrl
D14
D28
g
CAP marker gene
Gpihbp1
Kit
Ednrb
Car4
Ntrk2
Cd74
CAP1
CAP1_CAP2
CAP2
AT1-induced CAP
Avg. Expr.
% Expr.
h
AT1-induced CAP
TrkB+/Total CD31+ cells (%)
Ctrl
D14
D28
Cdc42^AT1-KO
i
Ctrl
Cdc42^AT1-KO D14
Cdc42^AT1-KO D28
TrkB ERG DAPI
j
Mechanical signals
AT1
AT2
CAP
Ntrk2+ CAP
Alveolar fibroblast

Figure 4

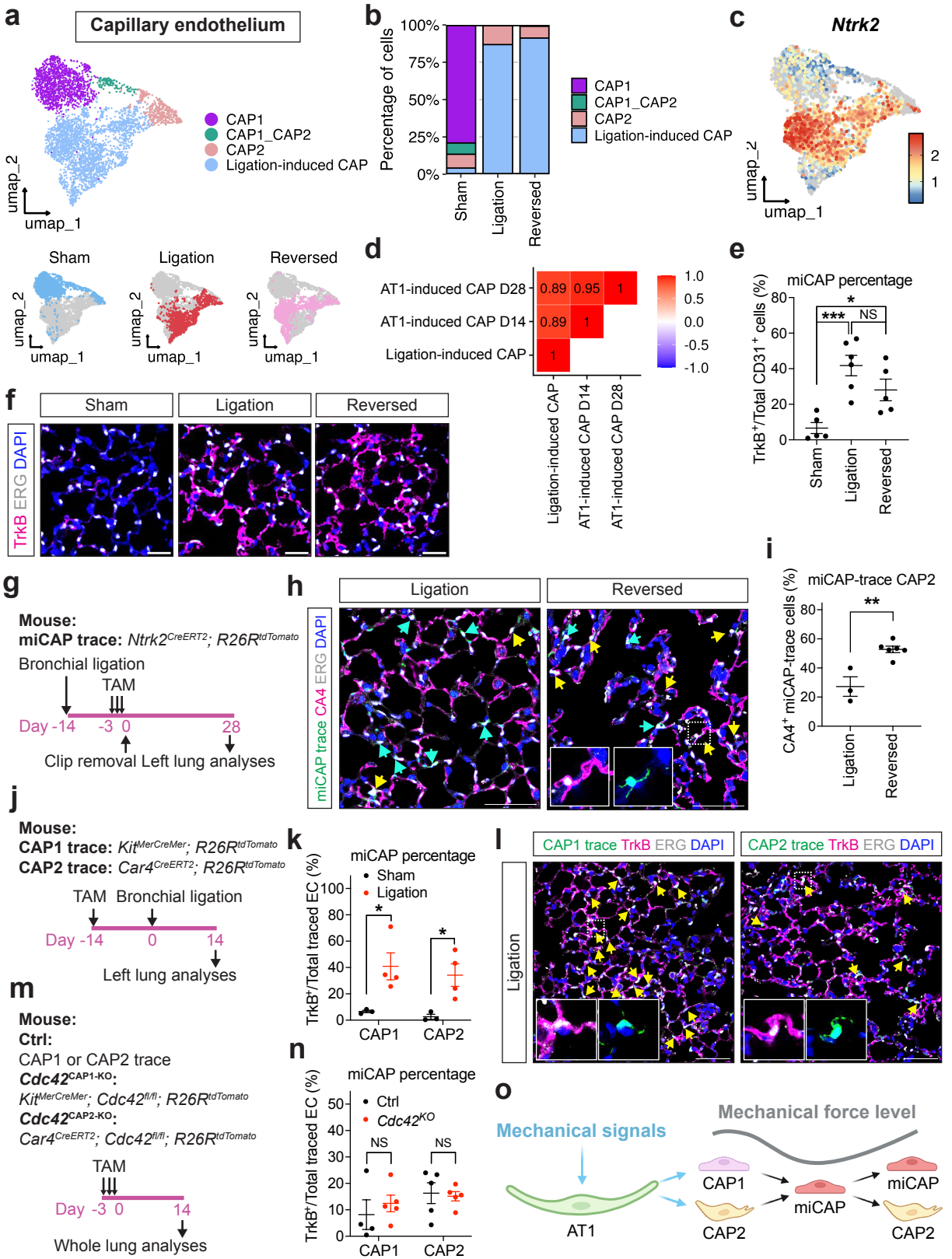
a
Capillary endothelium
CAP1
CAP1_CAP2
CAP2
Ligation-induced CAP
umap_2
umap_1
Sham
Ligation
Reversed
b
Percentage of cells
100%
75%
50%
25%
0%
Sham
Ligation
Reversed
c
Ntrk2
2
1
d
AT1-induced CAP D28
AT1-induced CAP D14
Ligation-induced CAP
0.89
0.95
1
1.0
0.5
0.0
-0.5
-1.0
e
miCAP percentage
TrkB+/Total CD31+ cells (%)
***
*
NS
f
TrkB ERG DAPI
g
Mouse:
miCAP trace: Ntrk2CreERT2; R26RtdTomato
Bronchial ligation
TAM
Day -14
-3 0
28
Clip removal Left lung analyses
h
miCAP trace CA4 ERG DAPI
i
miCAP-trace CAP2
CA4+ miCAP-trace cells (%)
**
j
Mouse:
CAP1 trace: KitMerCreMer; R26RtdTomato
CAP2 trace: Car4CreERT2; R26RtdTomato
TAM
Bronchial ligation
Day -14
0
14
Left lung analyses
k
miCAP percentage
Sham
Ligation
TrkB+/Total traced EC (%)
CAP1
CAP2
l
CAP1 trace TrkB ERG DAPI
CAP2 trace TrkB ERG DAPI
m
Mouse:
Ctrl:
CAP1 or CAP2 trace
Cdc42CAP1-KO:
KitMerCreMer; Cdc42fl/fl; R26RtdTomato
Cdc42CAP2-KO:
Car4CreERT2; Cdc42fl/fl; R26RtdTomato
TAM
Day -3 0
14
Whole lung analyses
n
miCAP percentage
Ctrl
Cdc42KO
NS
o
Mechanical signals
Mechanical force level
AT1
CAP1
CAP2
miCAP

Figure 5

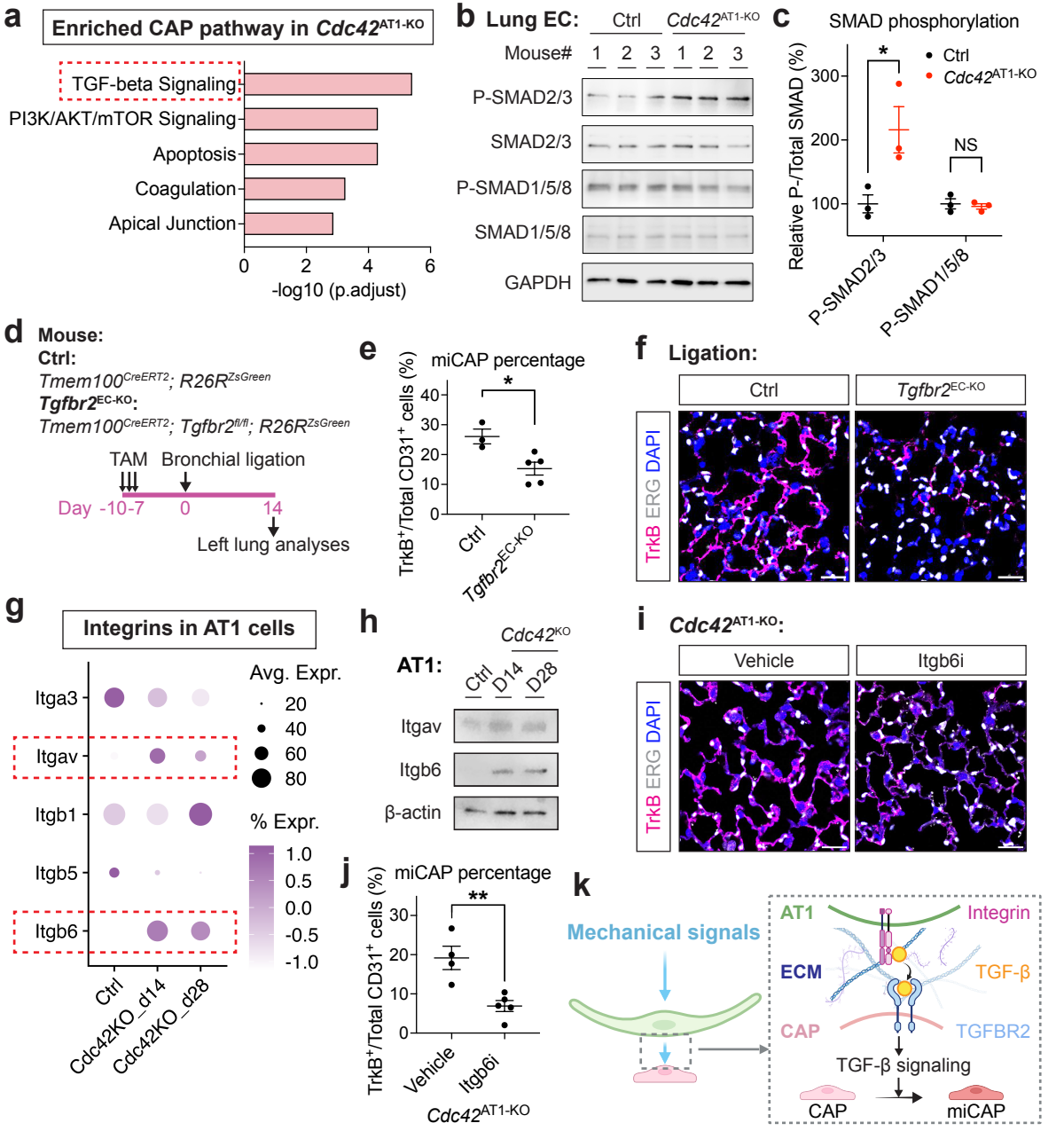
a
Enriched CAP pathway in Cdc42AT1-KO
TGF-beta Signaling
PI3K/AKT/mTOR Signaling
Apoptosis
Coagulation
Apical Junction
0
2
4
6
-log10 (p.adjust)
b
Lung EC:
Ctrl
Cdc42AT1-KO
Mouse#
1 2 3 1 2 3
P-SMAD2/3
SMAD2/3
P-SMAD1/5/8
SMAD1/5/8
GAPDH
c
SMAD phosphorylation
Relative P-/Total SMAD (%)
300
200
100
*
NS
Ctrl
Cdc42AT1-KO
P-SMAD2/3
P-SMAD1/5/8
d
Mouse:
Ctrl:
Tmem100CreERT2; R26RZsGreen
Tgfbr2EC-KO:
Tmem100CreERT2; Tgfbr2fl/fl; R26RZsGreen
TAM
Bronchial ligation
Day -10-7
0
14
Left lung analyses
e
miCAP percentage
TrkB+/Total CD31+ cells (%)
40
30
20
10
0
*
Ctrl
Tgfbr2EC-KO
f
Ligation:
Ctrl
Tgfbr2EC-KO
TrkB ERG DAPI
g
Integrins in AT1 cells
Avg. Expr.
20
40
60
80
% Expr.
1.0
0.5
0.0
-0.5
-1.0
Itga3
Itgav
Itgb1
Itgb5
Itgb6
Ctrl
Cdc42KO_d14
Cdc42KO_d28
h
Cdc42KO
AT1:
Ctrl
D14
D28
Itgav
Itgb6
β-actin
i
Cdc42AT1-KO:
Vehicle
Itgb6i
TrkB ERG DAPI
j
miCAP percentage
TrkB+/Total CD31+ cells (%)
30
20
10
0
**
Vehicle
Itgb6i
Cdc42AT1-KO
k
Mechanical signals
AT1
Integrin
ECM
TGF-β
CAP
TGFBR2
TGF-β signaling
CAP
miCAP

Figure 6

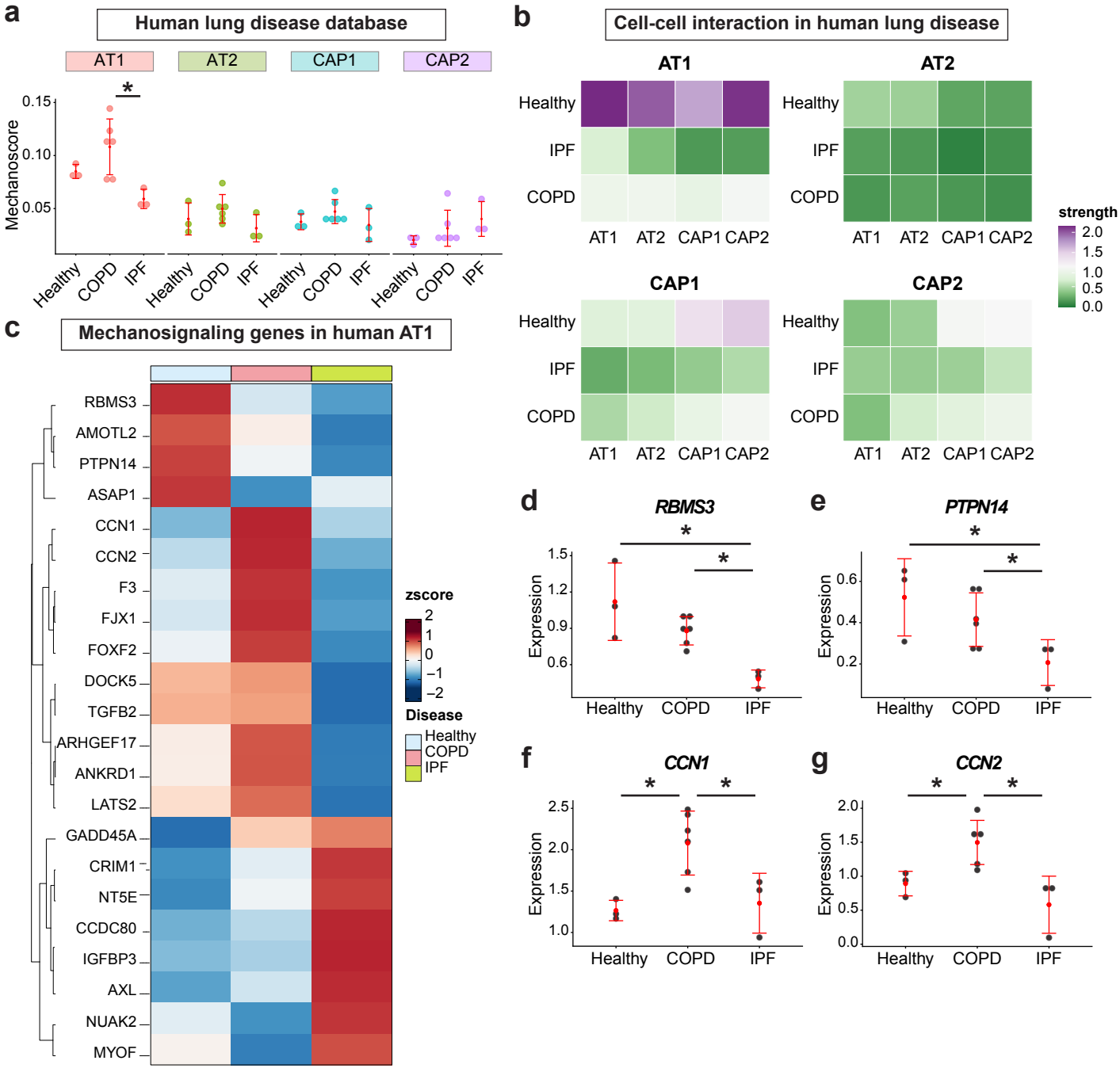
a
Human lung disease database
AT1
AT2
CAP1
CAP2
Mechanoscore
0.15
0.10
0.05
*
Healthy
COPD
IPF
b
Cell-cell interaction in human lung disease
AT1
AT2
CAP1
CAP2
Healthy
IPF
COPD
strength
2.0
1.5
1.0
0.5
0.0
c
Mechanosignaling genes in human AT1
RBMS3
AMOTL2
PTPN14
ASAP1
CCN1
CCN2
F3
FJX1
FOXF2
DOCK5
TGFB2
ARHGEF17
ANKRD1
LATS2
GADD45A
CRIM1
NT5E
CCDC80
IGFBP3
AXL
NUAK2
MYOF
zscore
2
1
0
−1
−2
Disease
Healthy
COPD
IPF
d
RBMS3
e
PTPN14
f
CCN1
g
CCN2
Expression

Extended Data Figure 1

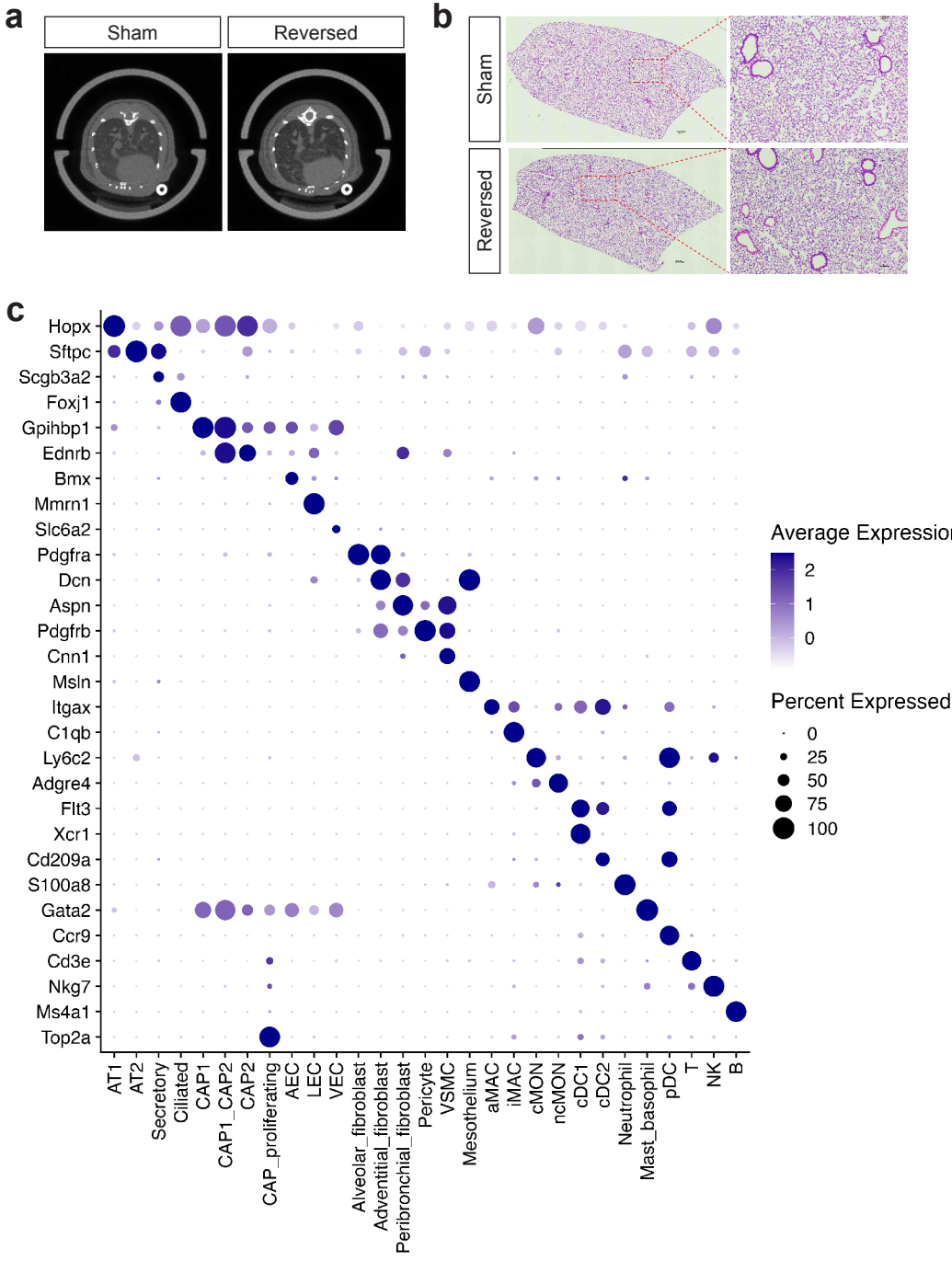

Extended Data Figure 2

a

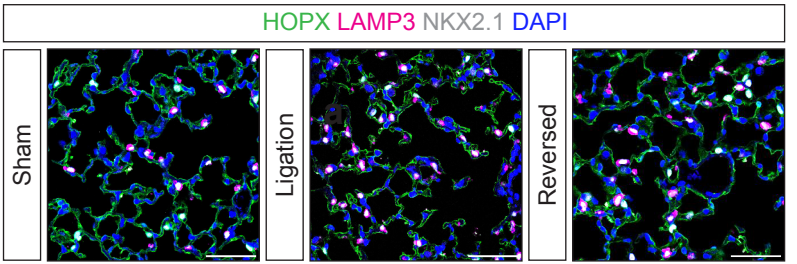

b

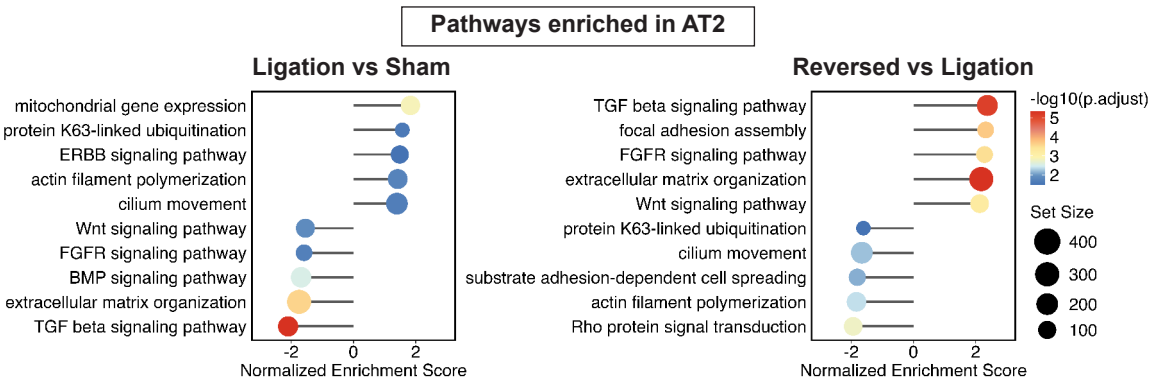

Extended Data Figure 3

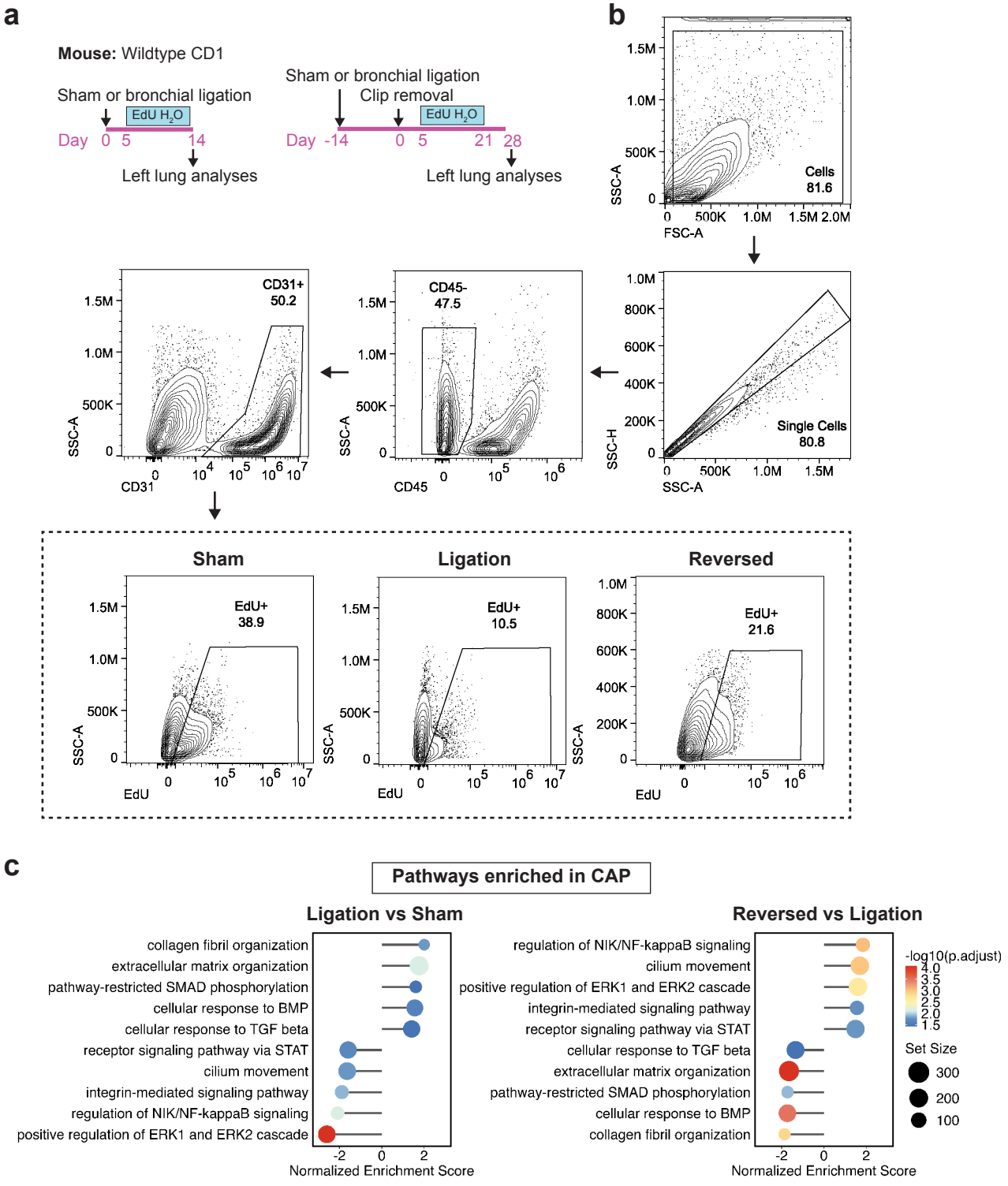

Extended Data Figure 4

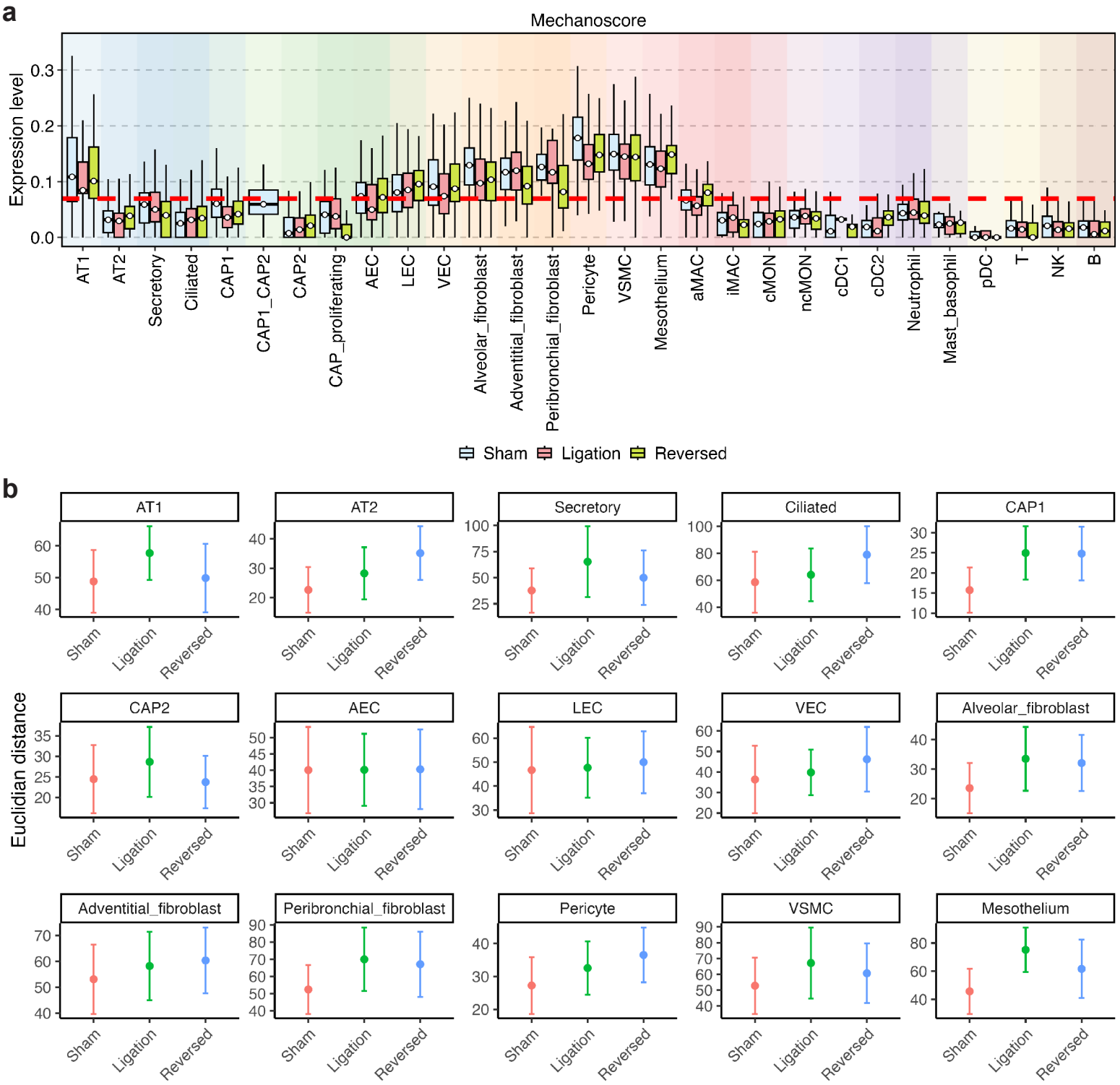

Extended Data Figure 5

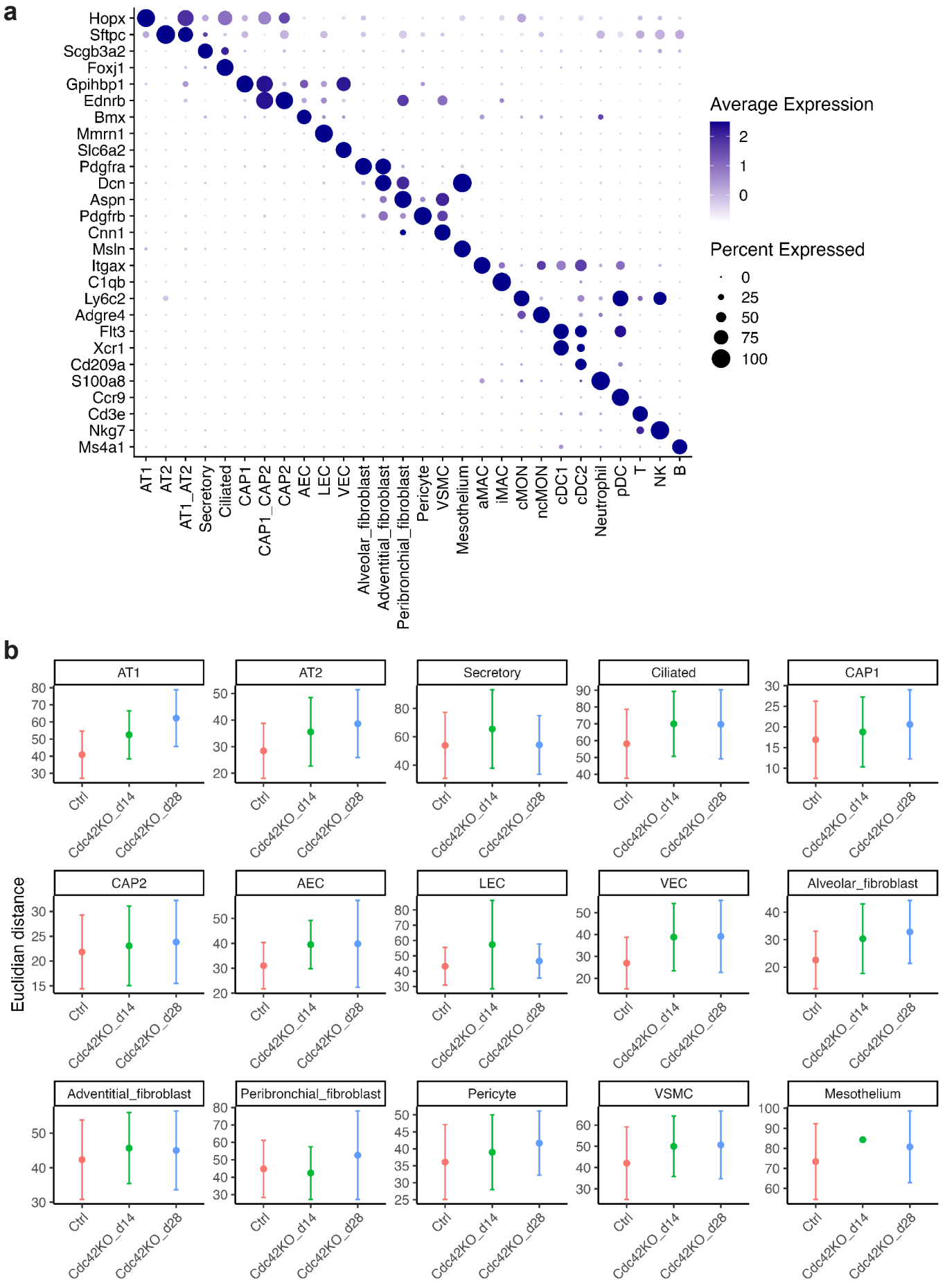

Extended Data Figure 6

a **CD45-, CD31+ lung cells:**

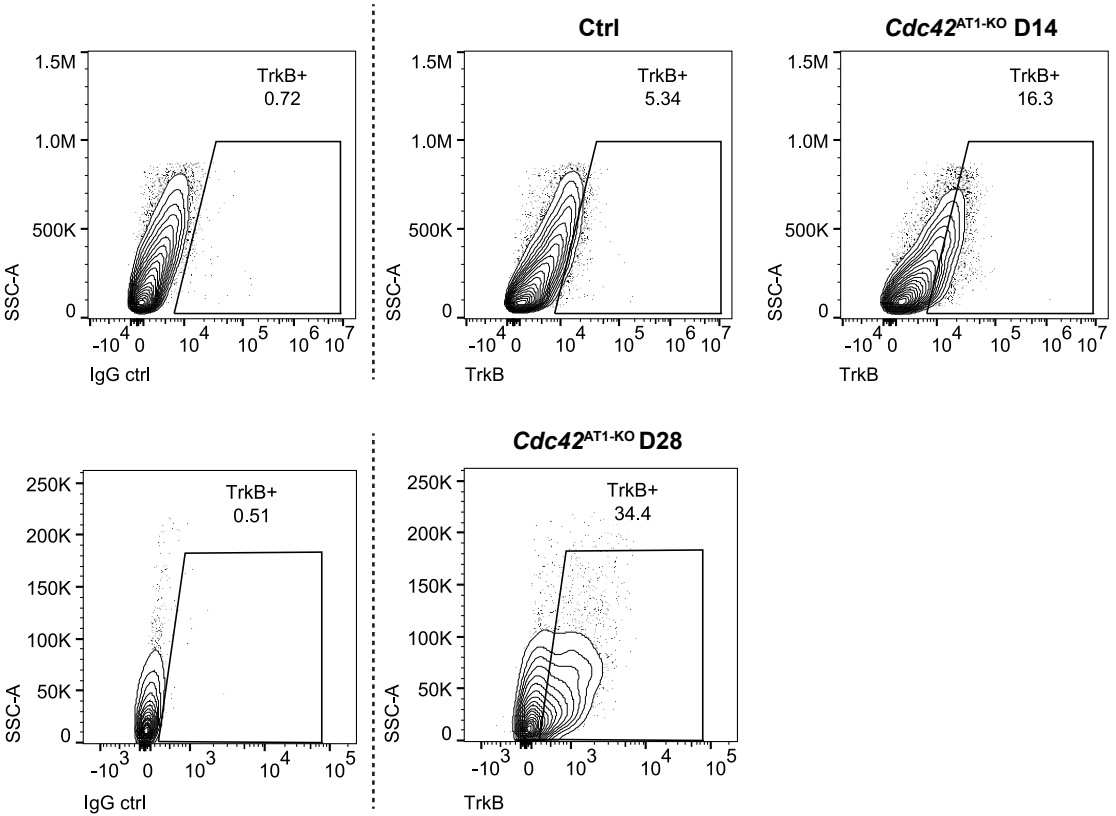

Extended Data Figure 7

a

Reversible ligation dataset

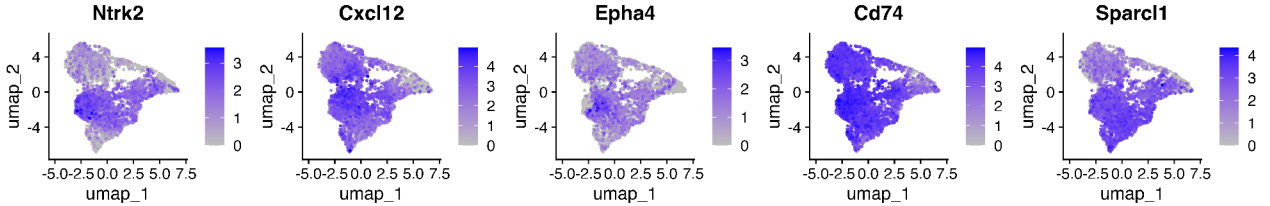

b

***Cdc42*$^{\text{AT1-KO}}$ dataset**

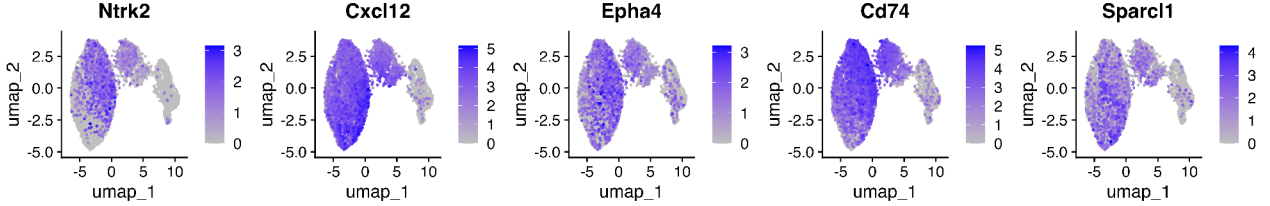

Extended Data Figure 8

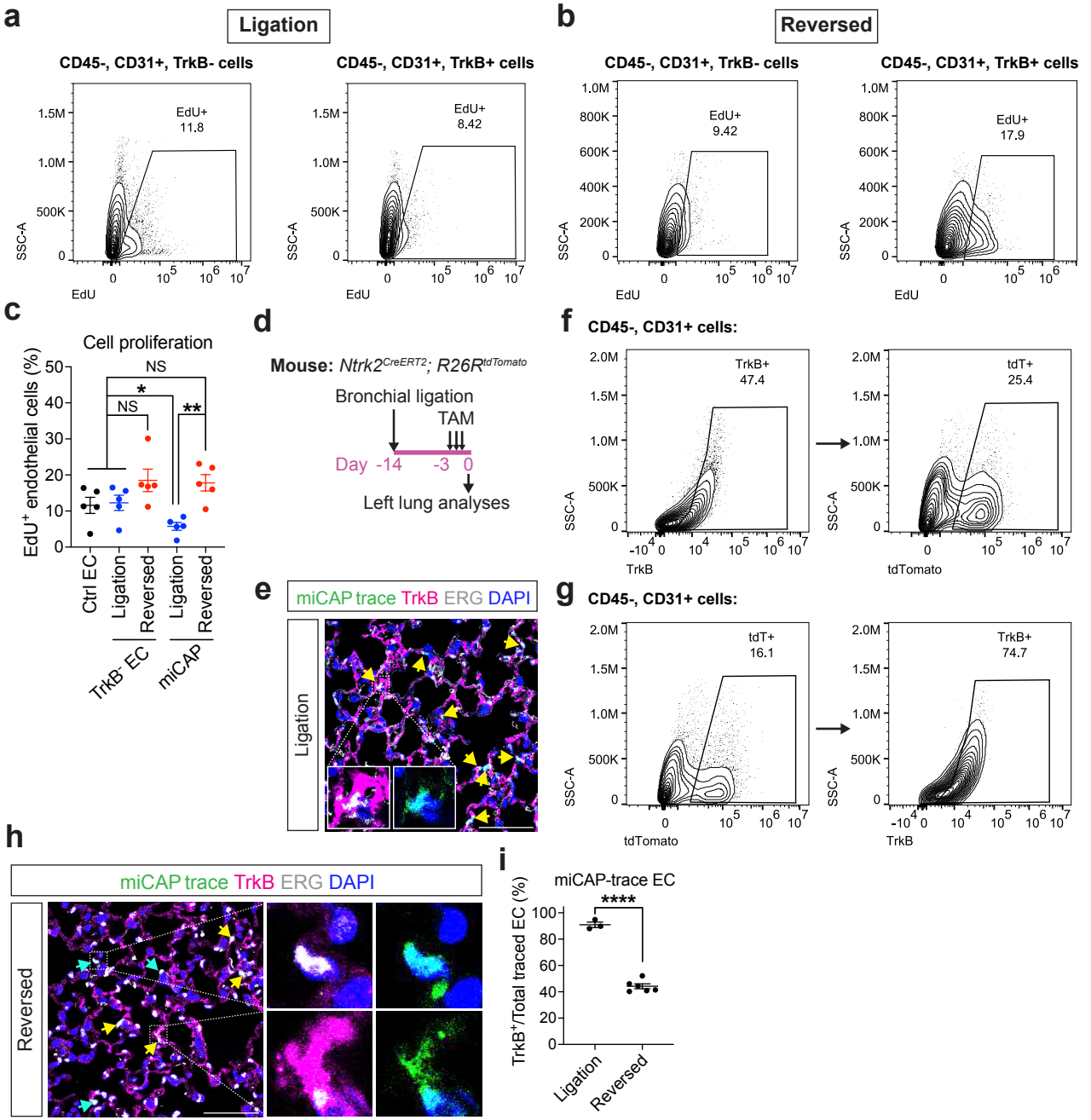

Extended Data Figure 9

a **CD45-, CD31+ cells in mouse lungs:**

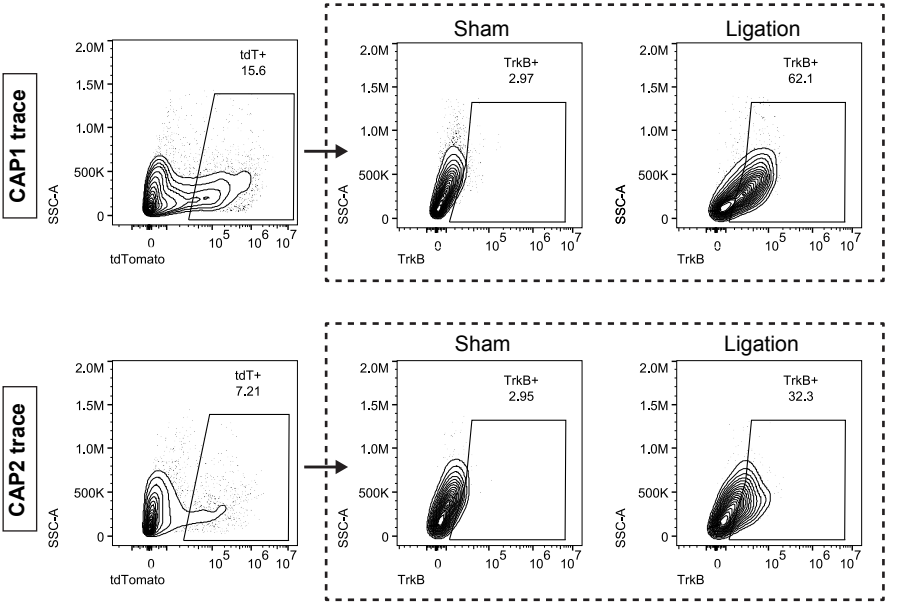

b

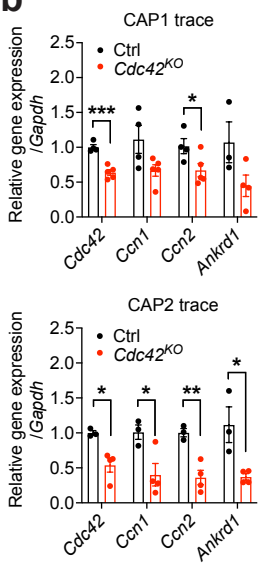

c **CD45-, CD31+, tdTomato+ cells in mouse lungs:**

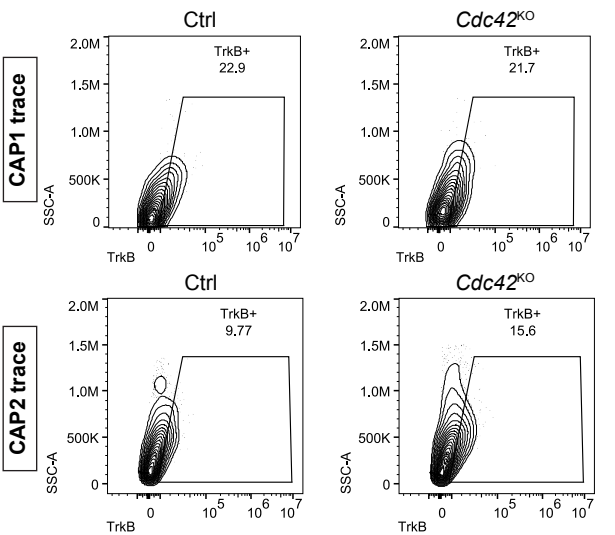

Extended Data Figure 10

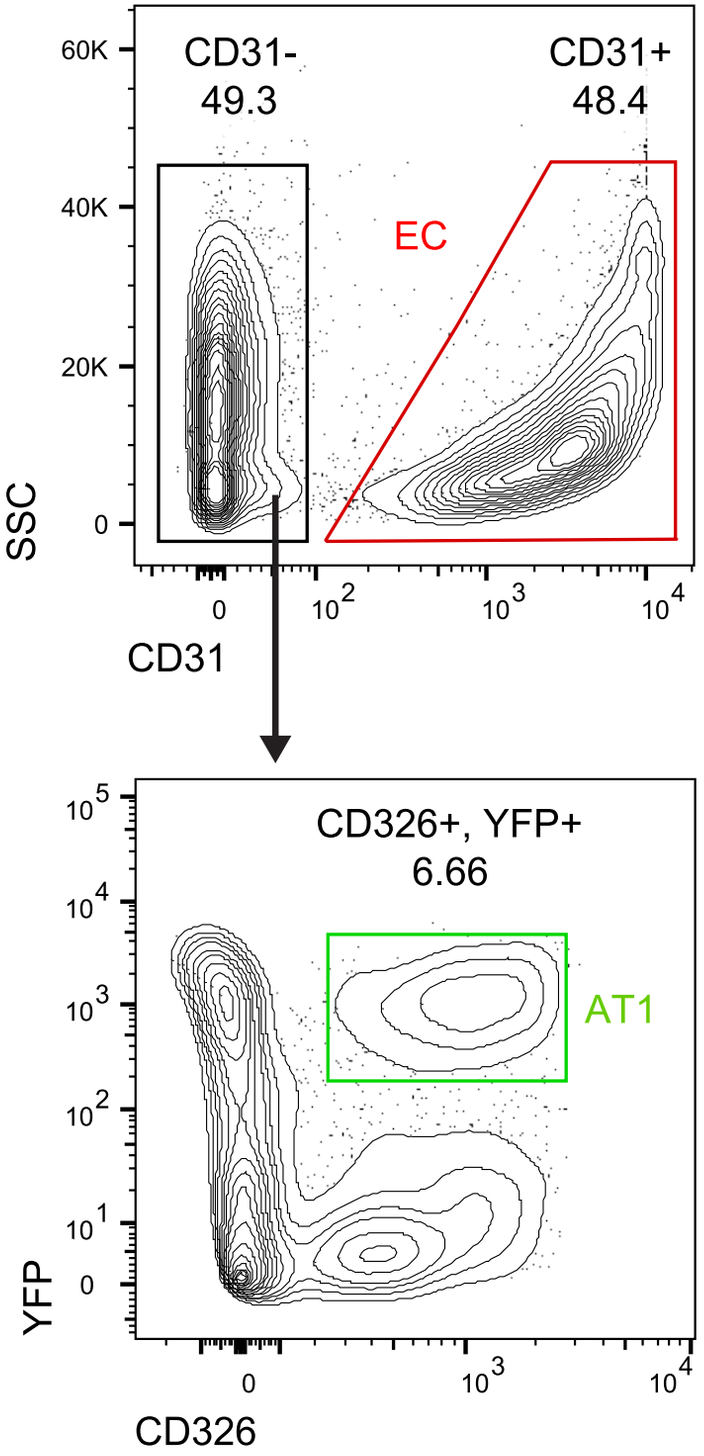

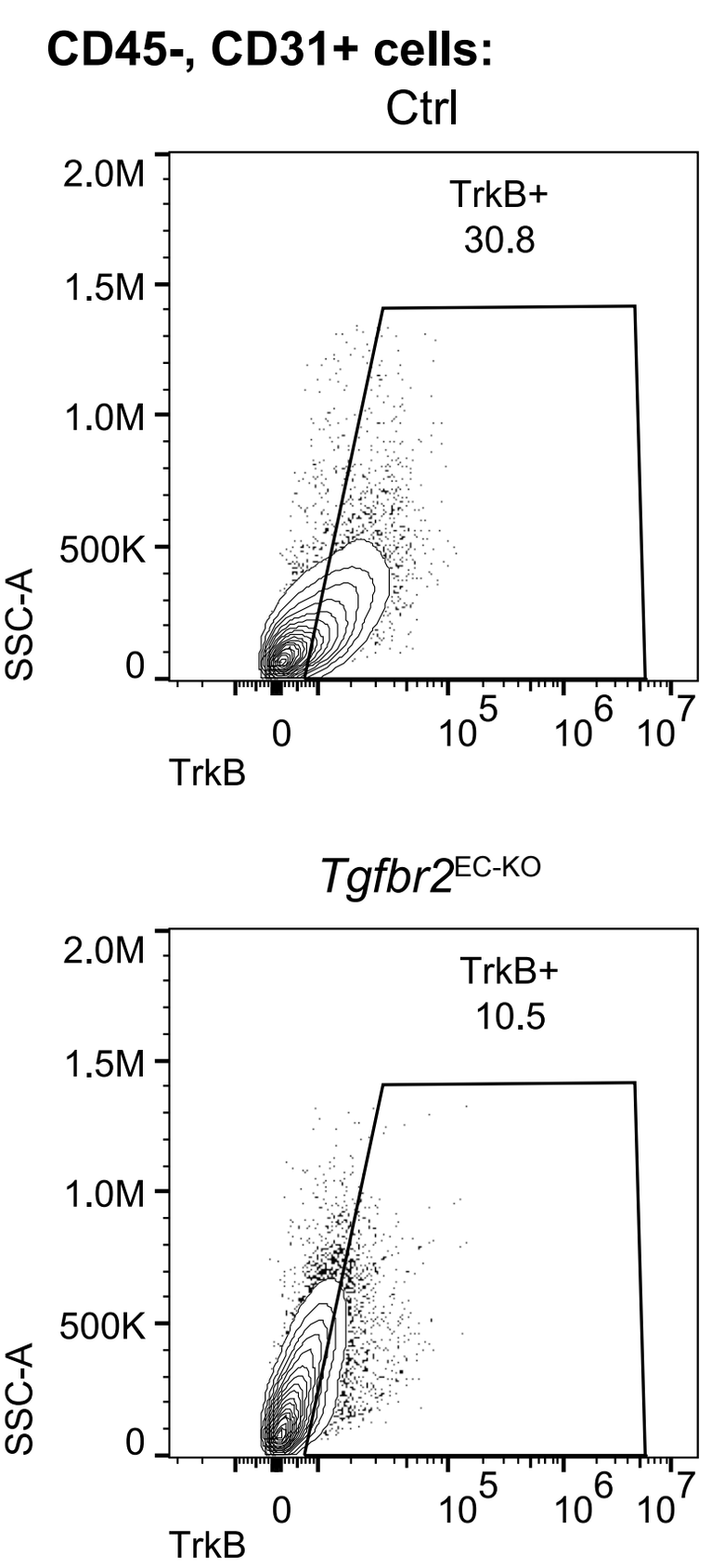

Extended Data Figure 11

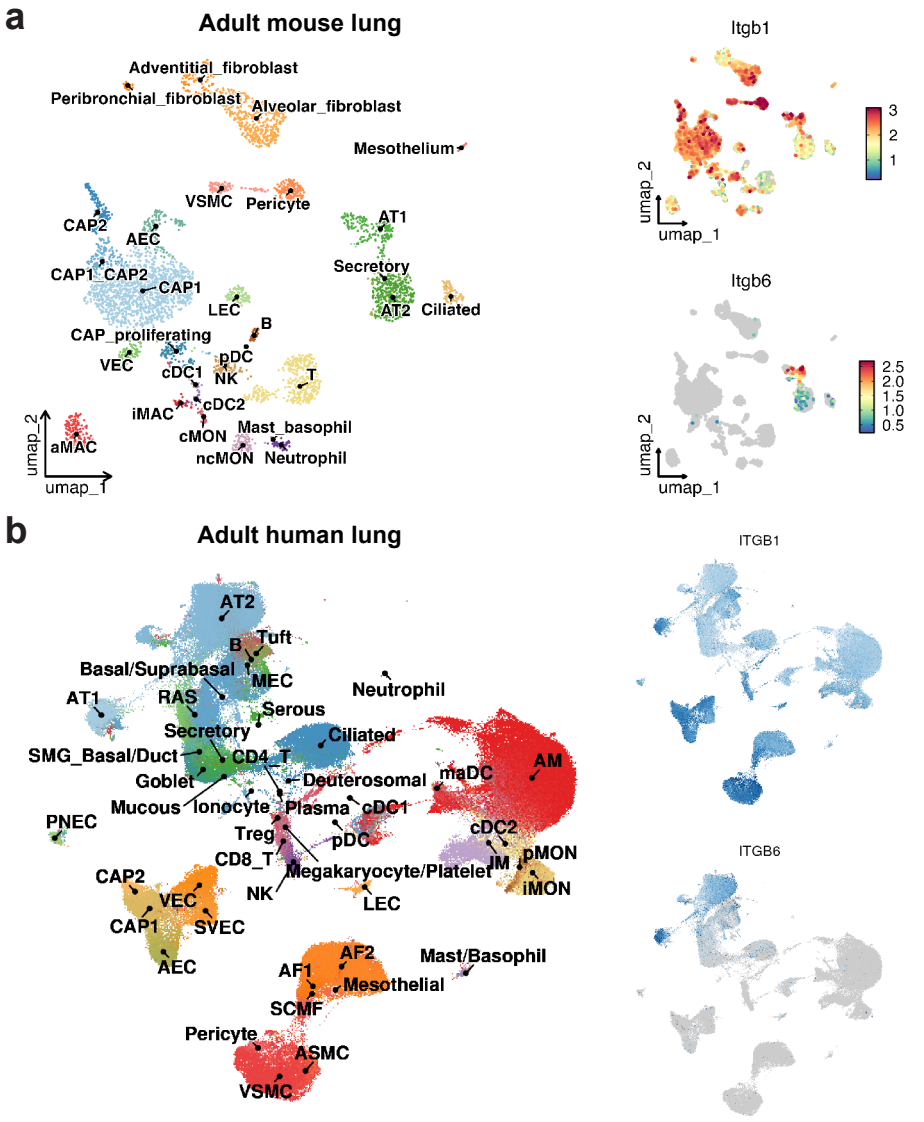
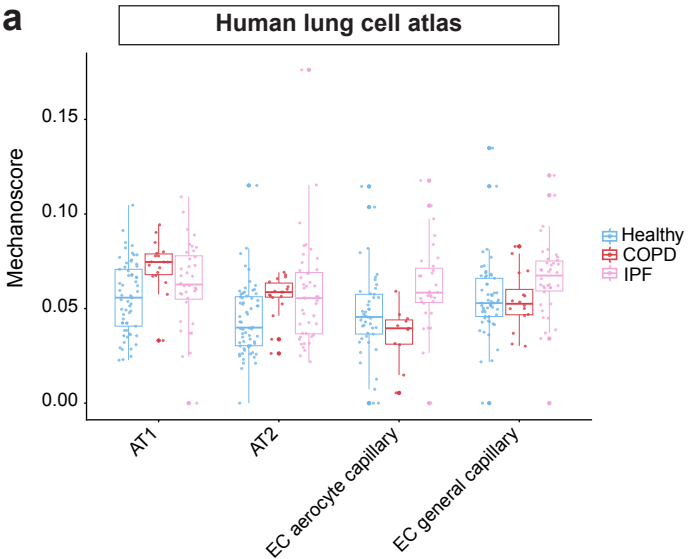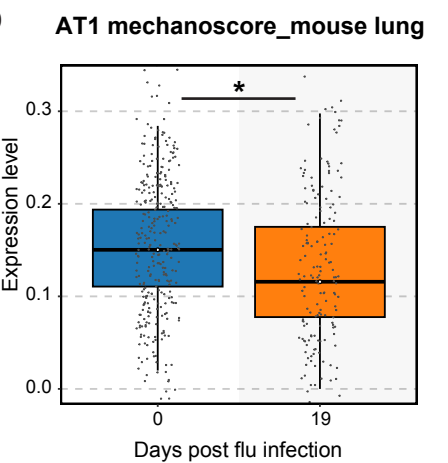
Extended Data Figure 12